Bachelor's thesis

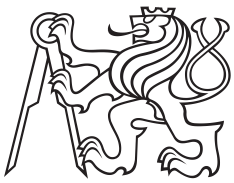

Czech Technical University in Prague

F3

Faculty of Electrical Engineering
Department of Control Engineering

# Modeling and control of a piezoelectric actuator for active and adaptive optics

**Marek Hudec**
Cybernetics and robotics

May 2013
Supervisor: Ing. Zdeněk Hurák, Ph.D.

# Acknowledgement / Declaration

I acknowledge a partial support provided by the Ministry of Education and Sports KONTAKT project no. 98028 based on international collaboration with teams at Harvard-Smithsonian Center for Astrophysics in Cambridge and NASA Goddard Space Flight Center. The other project is a more recent one under the Grant Agency of the Czech Republic, no. 13-33324S, aimed at development of X-ray optics.

I declare that the work presented here is, to the best of my knowledge and belief, original and the result of my own investigations, except as acknowledged. Formulations and ideas taken from other sources are cited as such.

Prague, 22 May 2013

.....

# Abstrakt / Abstract

V této práci jsou vypracovány matematické modely deformovatelných desek k použití v adaptivní a aktivní optice. Konkrétně se jedná o pozlacenou křemíkovou desku s nalepeným piezoelementem, pevně uchycenou na jedné straně. Modely jsou odvozeny analytickými postupy a metodou konečných prvků. Výsledky jsou porovnány s daty naměřenými pomocí laserového paprsku vychýleného na jednořádkovou CCD kameru. Nelineární jevy, jako jsou hystereze a creep, jsou pečlivě zhodnoceny a uvažovány v modelech. Ukázána je možnost řízení tvaru desek s piezoelementy.

**Klíčová slova:** deformovatelná, flexibilní, křemíková, deska, zrcadlo; piezoelektrický aktuátor, piezoelement; hystereze; model, řízení, deformace tvaru; aktivní, adaptivní optika.

**Překlad titulu:** Modelování a řízení piezoelektrického aktuátoru pro aktivní a adaptivní optiku

This thesis develops mathematical models of deformable plates used in adaptive and active optics. In particular, a Au-coated cantilevered plate made of silicon with a piezoelectric patch bonded to it is investigated. Models are derived using analytical techniques and finite element method. The results are compared to measurements obtained using a laser beam reflected to a line CCD camera. Nonlinear effects such as creep and hysteresis are carefully investigated and included in the model. Strategies for shape control are outlined.

**Keywords:** deformable, flexible, rectangular, silicon plate, mirror; piezoelectric actuator, patch, fiber composite; hysteresis; model, control, FEM shape, deformation; active, adaptive optics.

# Contents /

# Tables / Figures

# Chapter 1
# Introduction

This thesis focuses on controlled deformation of flat reflective surfaces (mirrors) used in active and adaptive optics. The topic has been very attractive in the research engineering community since controlled deformation can reduce impact of disturbances such as thermal and mechanical disturbance, imperfect manufacturing techniques, wavefront distortion etc. All these disturbances are unwelcome for the users of optical equipments and most of them cannot be fixed passively — i. e. by the means of a more precise manufacturing, filters or other methods that do not use actuators.

The field of actuated optics has got much attention recently; there have been hundreds of methods using dozens of different actuators implemented. Out of all these, in this thesis I will use a popular piezoelectric actuator. In particular, a fiber composite piezo patch (described in section 2.1.2) is used.

## 1.1 Active and adaptive optics

There are two approaches for non-passive elimination of the unwelcome disturbances — *adaptive* and *active* optics. Collectively I denote these as *actuated optics*.

Adaptive optics is a branch of actuation which covers disturbances with fast dynamics. It is used to compensate what is called an air optical disturbance. The moving air mass changes the wavefront and as a consequence, resulting images and measurements are distorted.

Active optics compensate a much slower or even static disturbances. It is used to compensate various sources of figure (and hence imaging) errors such as imperfect manufacturing and long-scale errors of relevant reflecting surfaces, imperfect adjustment on individual plates/substrates into modules, influences of gravity, heat, etc.

Thin piezoactuators allow for design of various types of deformable mirrors. While in optical (in visible light) it can lead to essential cost reductions for large aperture and/or space-based mirrors, there are also numerous applications in X-ray and XUV optics. The controllable bending (surface shaping/deformation) by active elements is expected to provide much better angular resolution of the relevant optical systems and modules. The active approach finds valuable applications also in other areas of X-ray imaging for many ground-based and laboratory applications, such as precise imaging in synchrotron beamlines, and in X-ray microscopes, with various applications in X-ray lithography, radiography, biology, medicine, material research, non-destructive testing, etc.

## 1.2 Motivation and goals

This thesis was motivated/inspired by a past research collaboration between a team at Czech Academy of Sciences and research teams at NASA Goddard Space Flight Center (GSFC) and Center for Astrophysics in Cambridge, MA (CfA). The research aimed

at development of active X-ray optics for US space mission called Generation-X. The idea was to significantly improve the angular resolution of future large imaging X-ray telescopes down to sub-arcsec values, impossible by all other (passive) methods and techniques.

From the experimental results obtained at that time it turned out that a more accurate modeling of piezoactuators was needed to achieve high-precision deformation of a surface. I was lucky to become part of the project, so I decided to continue exploring the possibilities of improving the mirrors resolution. In particular, the inspiration for my research came from the *Kirkpatrick-Baez* (KB) X-ray optics. Its purpose is to focus light in a reflective manner (figure 1.1). The lenses are made of a set of coated thin plates of different parabolic shapes. One such set is able to focus the X-rays in one dimension. The X-rays are generally reflected twice (using two perpendicularly aligned sets) to create focal images. Two KB modules (with thin silicon plates) developed in Prague are shown in figure 1.2.

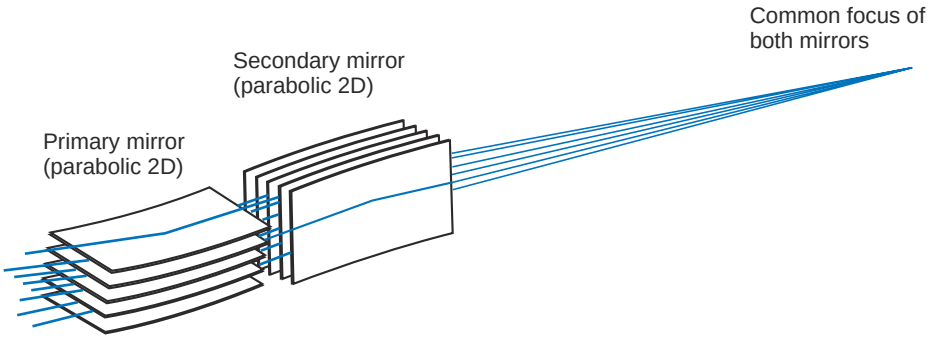


**Figure 1.1.** Kirkpatrick-Baez reflective lenses.

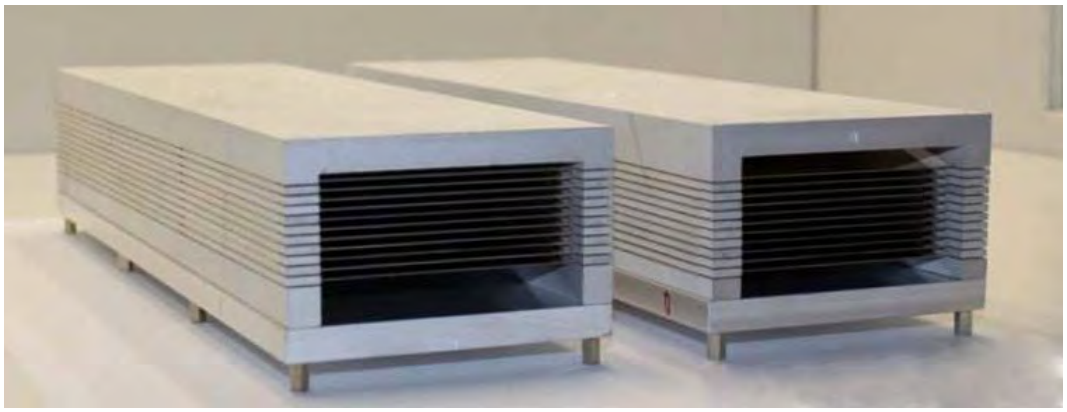

**Figure 1.2.** Two sets of thin parabolic plates used to focus X-rays developed at Rigaku Innovative Technologies Europe in Prague (taken from [1]).

The main goal of this work is to investigate and document suitable methods for modeling and analysis of piezoelectric monomorph plates for the purpose of surface shaping. The validity of the methods shall be demonstrated by laboratory experiments using a (provided) rectangular cantilever plate made of silicon with a commercially available piezoelectric patch bonded to it (figure 1.3). Particular attention in modeling shall be paid to practical nonlinear phenomena that occur in piezoelectric materials such as creep, hysteresis and depolarization. Based on the simulation and experimental outcome some challenges in control design are identified and basic compensation techniques are surveyed/proposed.

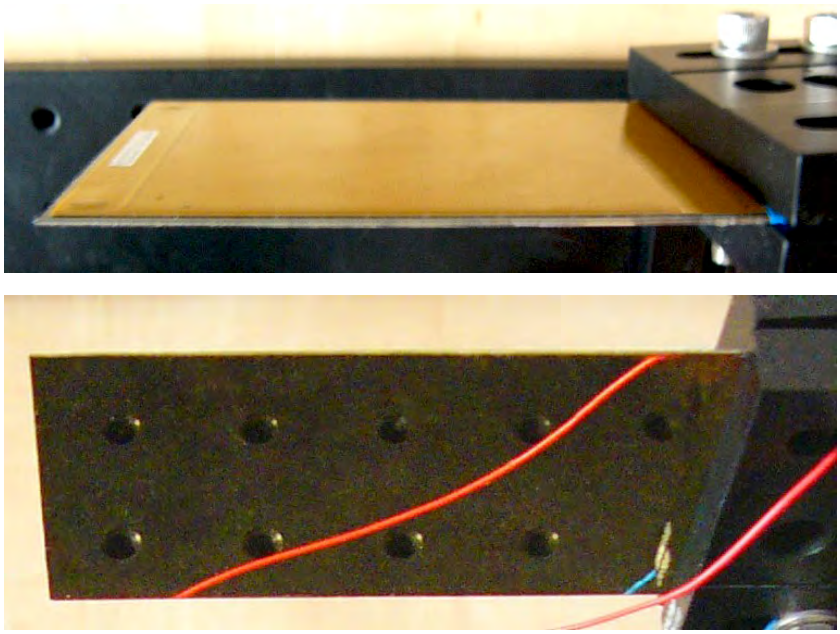

**Figure 1.3.** The coated monomorph cantilever plate. A patch piezoactuator on one side (upper image) and coated silicon wafer on the other (bottom image).

## 1.3 Outline of the thesis

The thesis starts by introducing the problem analyzed (chapter 2): the monomorph composition, description of the piezoactuator used including properties needed for the analysis. The analytical methods in chapter 3 are based on the mathematical description of the elasticity and piezoelectric effect (section 3.1). The analytical modeling section is structured into two main sections. The static behavior of the plate is modeled in the static analysis section (3.2). A case with more than one electrode will be included to show possibilities of controling the cantilever plate's shape. The dynamic analysis (section 3.3) is presented in modal form resulting from the Euler-Bernoulli beam equation.

Finite element methods (FEMs) are used to model the monomorph in chapter 4. I again decided to present static and dynamic methods separately. A nodal approach is presented in the static FEM section 4.2 and Comsol is used to simulate the cantilever static deflection (in 2D). The dynamic FEM is in section 4.3. The nodal form is converted into a modal form similar to that used in the analytical analysis and a general input-output model is shown (section 4.3.1). Comsol is used to find plate modes and corresponding frequencies in 4.3.2.

The cantilever plate's bending itself is assumed assumed linear (Hooke's law, constitutive relationships). A set of nonlinearities that I present in chapter 5 come from actuator and sensor subsystems. The actuator nonlinearities are that of the piezoelectric material (depolarization, creep and hysteresis) and those brought into the system by an imperfect amplifier. The hysteresis is modeled using the Prandtl-Ishlinskii model in section 5.3.2. The sensor nonlinearity, that comes from the setup, is described in section 5.5.

Response of the cantilever is measured at its tip. The measurements including response to initial conditions, modal response and hysteresis loops can be found in chapter 6. Arising control design issues are discussed in chapter 7. There are two sections in the

chapter, control of the piezoelectric actuator (including the nonlinearities presented) in section 7.1 and control for the use in adaptive/active optics (section 7.2).

Conclusions and ideas for future work are presented in the last chapter 8.

# Chapter 2
# Piezoelectric monomorph plate

The system I got to test and validate models derived in this thesis is a monomorph (sometimes called unimorph) piezoelectric plate. In order to analyze the piezoelectric monomorph, the geometry of it has to be described and a brief overview of its underlying physics must be done.

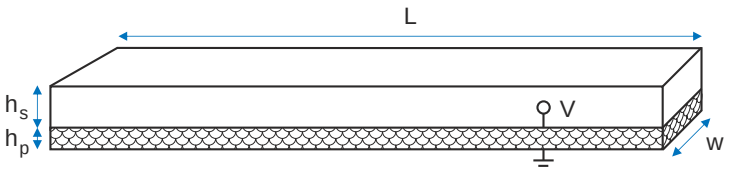


**Figure 2.1.** Piezoelectric monomorph plate.

The piezoelectric monomorph is in my case composed of 2 layers. The first one that will be called the *substrate* layer is made of pure silicon ⟨100⟩ (the three number 100 denote the crystallographic direction) coated by a thin golden layer. The coating is for the purpose of X-ray reflective optics. The second layer is a piezoelectric actuator, in my case MFC M-8557-P2, which will be described in 2.1.2.

The dimensions according to figure 2.1 are listed in table 2.1. I am also including the free length $l$ of the cantilevered monomorph, which is shorter than the total length $L$. The shorter length is due to the rigid clamp. It is needed for the analysis.

| Parameter | Value [mm] |
|---|---|
| $L$ | 100 |
| $l$ | 95.5 |
| $h_s$ | 0.7 |
| $h_p$ | 0.3 |
| $w$ | 63 |

**Table 2.1.** Monomorph dimensions.

## 2.1 Piezoceramics

Piezoceramic is a material used for manufacturing piezoelectric actuators. Many books like [2] and [3] describing the manufacturing process, the piezoceramic structure and underlying physics can be found. There is an effort to find new lead-free environment-friendly materials that would replace Pb in the world's dominating PZT actuators [4].

### 2.1.1 PZT

The PZT is a shorthand notation for a piezoelectric ceramic, that is popular thanks to its large $d$ coefficients of piezoelectric behavior and its relatively low price. The shorthand stands for $PbZrO_3$ - $PbTiO_3$ and is of perovskite type. Thanks to its tetragonal non-centrosymmetric structure, PZT exhibits piezoelectric effect [5].

### 2.1.2 Fiber composites

Instead of a monolithic ceramic, fibers are used for many actuators and sensors. Fibers are sealed in epoxy and interdigitated electrodes are used (figure 2.2). Fibers are popular not only for its cheap manufacturing, but mostly thanks to:

- interdigitated electrodes cause better strain performance, larger $d_{33}$ and $d_{31}$ constants;
- the multiphase structure of piezoceramic and polymer provides bending and twisting capability;
- volume fraction of piezoceramic can be controlled;
- electrodes can be positioned in a way to apply electric field in both poling direction and perpendicular to it (see figure 2.2).

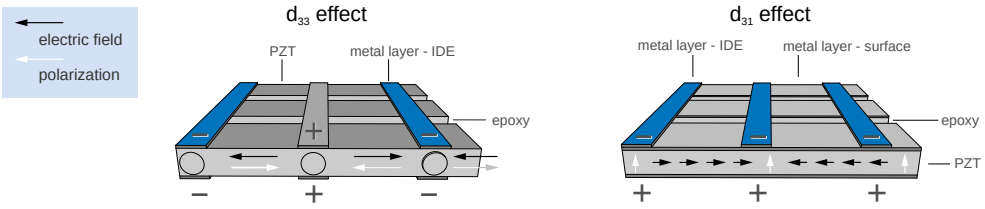


**Figure 2.2.** Interdigitated electrodes used in MFCs (taken from Smart Material[1]).

Piezoelectric fibers are embedded in a polymer phase (*polymer matrix*). Glass fibers (thinner than the ceramic fibers $\sim 5\,\mu$m) can be added for additional strength of the composite [6].

There are several patented materials on the market, including Macro Fiber Composite (MFC) invented by NASA and Active Fiber Composite (AFC) developed at the Active Materials and Structures Lab at MIT. The difference between these two is a manufacturing process. The final composite design is the same, consists of electrodes, fibers of piezoceramic and a polymer matrix.

The MFC in my case is composed of thin piezoelectric layers made of Sonox P505[2]). The P505 is used in MFC composites, it has properties similar to PZT-5A [7]. Parameters and its thermal dependency can be found in [8].

[1]) `www.smart-material.com`
[2]) `www.ceramtec.com`

## 2.2 Layers

The monomorph is actually not composed of only the two layers. The fact that the MFC itself is composed of active and passive layers must be taken into account. I need to consider it to obtain exact models. The active width if the MFC is 180 $\mu$m only, which is almost half the actual width of the actuator (300 $\mu$m). The real composition of the plate is shown in figure 2.3.

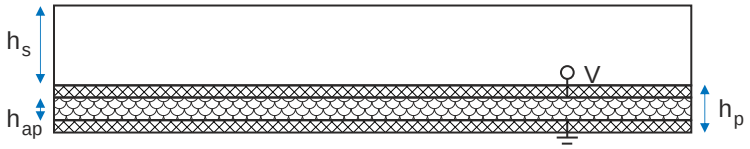


**Figure 2.3.** Actual layers of the piezoelectric monomorph plate.

The width of the active piezoelectric layer completes the table 2.1:

$$h_{ap} = 180\,\mu\text{m}. \tag{1}$$

## 2.3 Material characteristics

The parameters listed in table 2.2 describe electromechanical characteristics of the monomorph plate. The parameters of the silicon wafer were taken from [9]. Piezoelectric properties were taken from [8], MFC properties from [10].

The value of $\rho$ of the whole plate and must be averaged for densities listed in table 2.2. I obtained a rough value as

$$\rho = 0.3\,\rho_{mfc} + 0.7\,\rho_s = 3110\,\text{kg}\cdot\text{m}^{-3}, \tag{2}$$

where $\rho_{mfc} = 5000\,\text{kg}\cdot\text{m}^{-3}$ is an average density of the MFC actuator.

| Parameter | Notation | Value |
|---|---|---|
| Young's modulus of Si | $Y_s$ | 130 GPa |
| Young's modulus of MFC | $Y_p$ | 30 GPa |
| Poisson's ratio of Si | $\nu_s$ | 0.064 |
| Poisson's ratio of MFC | $\nu_p$ | 0.31 |
| Coupling constant $d_{31}$ | $d_{31}, d_{13}$ | -180 pm/V |
| Coupling constant $d_{33}$ | $d_{33}$ | 475 pm/V |
| Density of MFC's piezoceramic | $\rho_p$ | 5440 kg/cm$^3$ |
| Density of Si (20° C) | $\rho_s$ | 2300 |
| Relative permittivity of MFC | $\epsilon_p$ | 1800 |
| Capacitance of M-8557-P2 | $C_p$ | 402 nF |

**Table 2.2.** Mechanical and electrical properties of materials used.

# Chapter 3
# Analytical models

An analytical model useful for not only the adaptive/active optics will be derived. The models should be simple enough for the use in control. I will go through the static and dynamic response (sections 3.2 and 3.3) of the monomorph piezoelectric plate. In order to analyze the piezoelectric monomorph, an overview of the quantities and parameters and its underlying physics must be done.

## 3.1 Mathematical description

### 3.1.1 Stress and strain

Mechanical properties of a deformable body are mathematically described by two third-rank tensors. The first is the stress and describes a pressure applied not only along the main three axises, but also includes the shear stresses. The true origin is the pressure and because the stress is strictly directional it is always related to an oriented infinitesimally small surface d**A**. Normal stress is the stress that is normal to the area d**A** and is obtained simply by taking the normal force **F** and dividing it by the area. Infinitesimally I get

$$\sigma_n = \frac{\mathrm{d}F_n}{\mathrm{d}A}.$$

The shear (or plane) stress completes the information by taking forces that act in the d**A** plane (perpendicular to the normal force) into account. The complete stress matrix contains 9 stress components (visualized in figure 3.1):

$$\boldsymbol{\sigma} = \begin{pmatrix} \sigma_{11} & \sigma_{12} & \sigma_{13} \\ \sigma_{21} & \sigma_{22} & \sigma_{23} \\ \sigma_{31} & \sigma_{32} & \sigma_{33} \end{pmatrix}.$$

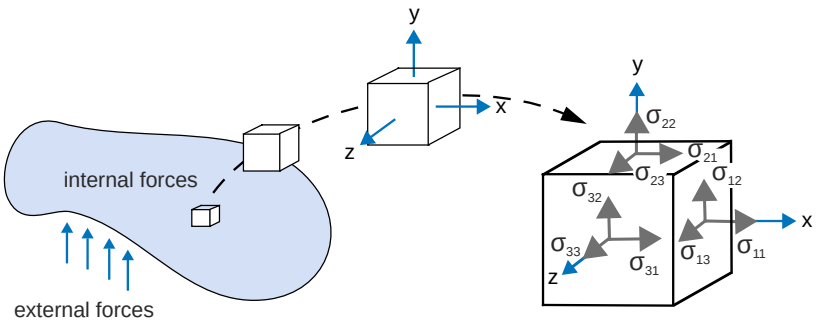


**Figure 3.1.** Geometrical representation of the stress matrix.

The second third-rank tensor is the strain. It describes the deformation itself. A point of an elastic body changes its position in case of an applied stress (the exact change depends not only on the stress, but also on boundary conditions). The shift in position can be described by a vector visualized in figure 3.2. The vector is called the displacement vector and is denoted $\mathbf{u} = (u_1, u_2, u_3)$.

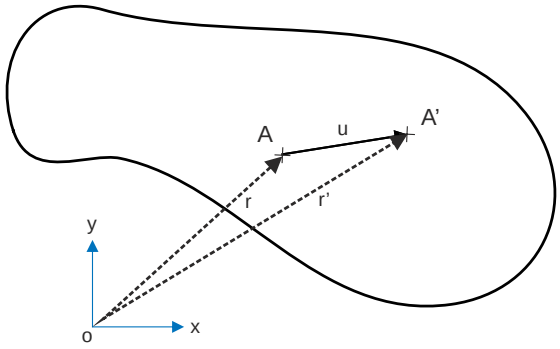


**Figure 3.2.** Geometrical representation of the displacement.

The complete strain tensor comprises 9 terms:

$$\boldsymbol{\epsilon} = \begin{pmatrix} \epsilon_{11} & \epsilon_{12} & \epsilon_{13} \\ \epsilon_{21} & \epsilon_{22} & \epsilon_{23} \\ \epsilon_{31} & \epsilon_{32} & \epsilon_{33} \end{pmatrix}.$$

The diagonal (principal) strains are those that occur along the main axises (elongations). The off-diagonal terms represent shear strains and their geometrical meaning is shown in figure 3.3.

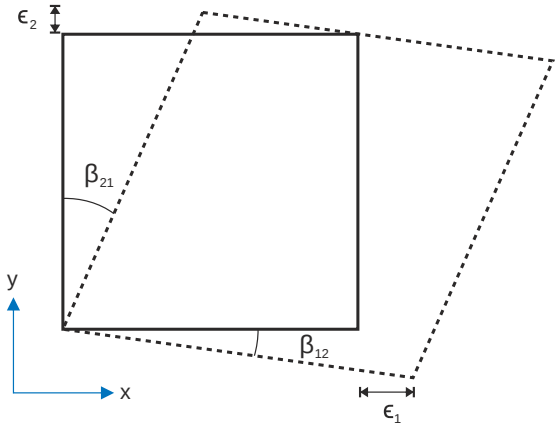


**Figure 3.3.** Geometrical representation of strain (two dimensions).

The infinitesimal strain theory, which is valid only for small strains, approximates the strain-displacement relation as

$$\epsilon_{ij} = \frac{1}{2}\left(\frac{\partial u_i}{\partial x_j} + \frac{\partial u_j}{\partial x_i}\right) \tag{1}$$

for $i, j = 1, 2, 3$, where $x_k$ is the $k$-th coordinate axis ($x_1 \equiv x, x_2 \equiv y, x_3 \equiv z$) [11].

Both the strain and the stress tensors are symmetric, meaning

$$\epsilon_{ij} = \epsilon_{ji}, \quad \sigma_{ij} = \sigma_{ji}. \tag{2}$$

Thanks to symmetry a simplified notation that uses 6 component vectors instead of tensors can be used [12]. The stress and strain are represented by vectors

$$\mathbf{S} = \begin{pmatrix} S_1 \\ S_2 \\ S_3 \\ S_4 \\ S_5 \\ S_6 \end{pmatrix}, \qquad \mathbf{T} = \begin{pmatrix} T_1 \\ T_2 \\ T_3 \\ T_4 \\ T_5 \\ T_6 \end{pmatrix},$$

where

$$\begin{aligned} S_1 &= \epsilon_{11} = \frac{\partial u_1}{\partial x_1}, & T_1 &= \sigma_{11}, \\ S_2 &= \epsilon_{22} = \frac{\partial u_2}{\partial x_2}, & T_2 &= \sigma_{22}, \\ S_3 &= \epsilon_{33} = \frac{\partial u_3}{\partial x_3}, & T_3 &= \sigma_{33}, \\ S_4 &= 2\epsilon_{23} = \frac{\partial u_2}{\partial x_3} + \frac{\partial u_3}{\partial x_2}, & T_4 &= \sigma_{23}, \\ S_5 &= 2\epsilon_{13} = \frac{\partial u_1}{\partial x_3} + \frac{\partial u_3}{\partial x_1}, & T_5 &= \sigma_{13}, \\ S_6 &= 2\epsilon_{12} = \frac{\partial u_1}{\partial x_2} + \frac{\partial u_2}{\partial x_1}, & T_6 &= \sigma_{12}. \end{aligned} \tag{3}$$

### 3.1.2 Constitutive relationships

The two basic relations are those between the stress $\mathbf{T}$ and strain $\mathbf{S}$ and between the electric field $\mathbf{E} = (E_1\ E_2\ E_3)^T$ and electric displacement $\mathbf{D} = (D_1\ D_2\ D_3)^T$. The relations were found empirically and are valid for most of the cases (low temperatures, electric fields and stresses) [12]. A material that undergoes stress can be described by a linear equation

$$\mathbf{S} = \mathbf{c}\mathbf{T} \tag{4}$$

known as the Hooke's law. The matrix $\mathbf{c}$ characterizes compliance of the material. The larger the compliance value is the larger strain is obtained by applying same stress. A dielectric that is exposed to electric field can be described by a similar relation

$$\mathbf{D} = \varepsilon\mathbf{E}. \tag{5}$$

The matrix $\varepsilon$ is called the permittivity and characterizes (permits) electric field behavior in dielectrics. High permittivity causes high electric flux in the material.

According to (4) and (5) there are just two matrices that characterize the material's behavior. The relations can generally differ from one direction to another:

$$\mathbf{c} = \begin{pmatrix} c_{11} & c_{12} & c_{13} & c_{14} & c_{15} & c_{16} \\ c_{21} & c_{22} & c_{23} & c_{24} & c_{25} & c_{26} \\ c_{31} & c_{32} & c_{33} & c_{34} & c_{35} & c_{36} \\ c_{41} & c_{42} & c_{43} & c_{44} & c_{45} & c_{46} \\ c_{51} & c_{52} & c_{53} & c_{54} & c_{55} & c_{56} \\ c_{61} & c_{62} & c_{63} & c_{64} & c_{65} & c_{66} \end{pmatrix}, \qquad \boldsymbol{\varepsilon} = \begin{pmatrix} \varepsilon_{11} & \varepsilon_{12} & \varepsilon_{13} \\ \varepsilon_{21} & \varepsilon_{22} & \varepsilon_{23} \\ \varepsilon_{31} & \varepsilon_{12} & \varepsilon_{33} \end{pmatrix}.$$

For a material that is piezoelectric both the electrical and mechanical descriptions apply. The linear coupled relation is

$$\mathbf{S} = \mathbf{c}_E \mathbf{T} + \mathbf{d}\mathbf{E}, \tag{6}$$

$$\mathbf{D} = \mathbf{d}^T \mathbf{T} + \varepsilon_T \mathbf{E}. \tag{7}$$

The piezoelectric coefficient matrix $\mathbf{d}$ gives an idea of how piezoelectric the material really is. Important characteristic of all the piezoelectric materials is the fact that the coefficient matrix $\mathbf{d}$ is same for both direct and transverse piezoelectric effect. The superscript $T$ indicates transposition. The subscripts indicate that the coefficient is the same as if there was no piezoelectric effect — i. e. when it is (the coefficient) measured, all variables that might influence the measurement results are held constant. Here it is the electric field $\mathbf{E}$ being held constant, so the measured uninfluenced compliance matrix $\mathbf{c}$ is denoted $\mathbf{c}_E$).

There is only one independent coefficient $d$ for a piezoelectric material that is homogeneous and isotropic. But in general it is

$$\mathbf{d} = \begin{pmatrix} d_{11} & d_{12} & d_{13} \\ d_{21} & d_{22} & d_{23} \\ d_{31} & d_{32} & d_{33} \\ d_{41} & d_{42} & d_{43} \\ d_{51} & d_{52} & d_{53} \\ d_{61} & d_{62} & d_{63} \end{pmatrix}.$$

## 3.2 Static analysis

I will now analyze the shape obtained by applying certain voltage across the piezoelectric layer. For simplicity, the plate will be represented by a two-dimensional beam clamped on one end and free on the other. As if the piezoelectric layer had no electromechanical coupling in the direction that I have just neglected. The assumed geometry can be seen in figure 3.4. The thin cantilever (beam) can ideally be described by a one-dimensional equation of motion.

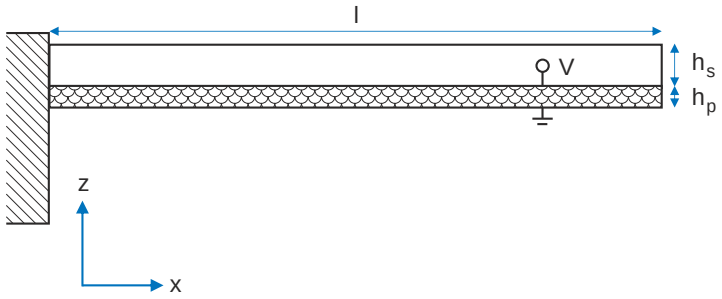


**Figure 3.4.** Geometry of a cantilevered plate used for static analysis.

The electric field **E** is reduced to one dimension only:

$$E_1 = E_2 = 0, \tag{8}$$

$$E_3 = \frac{V}{h_p}. \tag{9}$$

The vector of stresses has only one non-zero component:

$$T_2 = \cdots = T_6 = 0. \tag{10}$$

Not including shear strains I am left with only a few equations coming from the constitutive relationships (6), (7):

$$S_1 = \frac{1}{Y_1} T_1 + d_{13} E_3, \tag{11}$$

$$S_2 = -\frac{\nu_{21}}{Y_1} T_1 + d_{23} E_3, \tag{12}$$

$$S_3 = -\frac{\nu_{31}}{Y_1} T_1 + d_{33} E_3. \tag{13}$$

From the matrix symmetry similar to (2) $d_{31} = d_{13}$ the only relationship, for $D_3$, is

$$D_3 = d_{31} T_1 + \epsilon_{33} E_3. \tag{14}$$

A handy representation of the relationships are the resulting blocked stress (15) and free strain (16) easily obtainable from the relationships above:

$$T_1\Big|_{S_1=0} = -d_{13} Y_1 E_3, \tag{15}$$

$$S_1\Big|_{T_1=0} = d_{13} E_3. \tag{16}$$

What is more useful in adaptive optics is the free strain rather than the blocked force. Plugging the geometry of my problem

$$S_1 = \frac{u_1}{L}, \tag{17}$$

$$E_3 = \frac{V}{h_p} \tag{18}$$

into (16) I get a relationship describing free displacement of a non-bonded piezoelectric layer ($T_1 = 0$)

$$u_1\Big|_{T_1=0} = \frac{Ld_{13}}{h_p}V. \tag{19}$$

The MFC actuator in my case can extend up to displacements calculated in table 3.1.

| Voltage $V$ [V] | 10 | 50 | 100 | 300 |
|---|---|---|---|---|
| Free displ. $u_1$ [$\mu$m] | -0.48 | -2.41 | -4.82 | -14.45 |

**Table 3.1.** Free displacement of MFC M-8557-P2.

Bonding the actuated piezoelectric layer to a substrate layer causes stress in the material resulting in a nonzero bending moment. The piezoelectric layer contracts (due to the $d_{31}$ effect) and the beam thus deflects its tip downwards (according to figure 3.4). An element being bent is shown in figure 3.5. I will use a Euler-Bernoulli assumption that plane sections remain plane after bending.

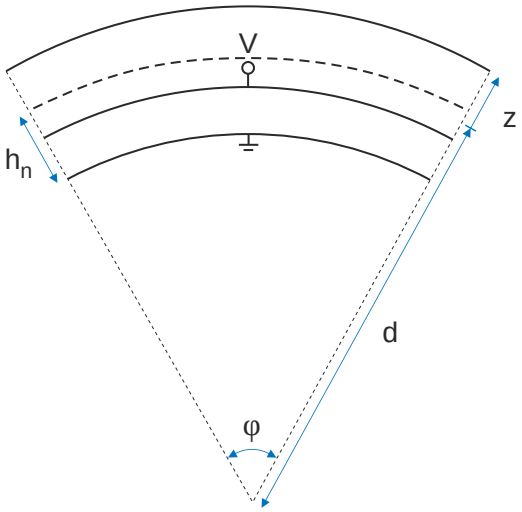


**Figure 3.5.** Element of a beam that is being bent.

The neutral axis is the dashed line in figure 3.5. It is characterized by zero stress and strain along it. In other words, its length stays the same after bending. A position of the neutral axis is different for different thicknesses and materials used. A stiffer material tends to place the neutral axis in it's thickness middle. In my case it is the silicon wafer that is much more stiff than the MFC; the neutral axis takes place in the upper half of the monomorph.

The exact position (distance from the bottom edge of the piezoelectri layer) [13] is given by

$$h_n = -\frac{\left(\frac{h_p^2}{Y_p} + \frac{h_s^2}{Y_s}\right) - 2\left(\frac{h_p}{Y_p} + \frac{h_s}{Y_s}\right)(h_p + h_s)}{2\left(\frac{h_p}{Y_p} + \frac{h_s}{Y_s}\right)}. \tag{20}$$

The calculated value for the my case is listed in table 6.1.

Distance from the neutral axis (in the direction shown in figure 3.5) is denoted $z$. Based on the figure 3.5 a strain-curvature relationship can be derived

$$S_1(z) = \frac{(d+z)\varphi - d\varphi}{d\varphi} = \frac{z}{d} = \kappa z, \tag{21}$$

where $\kappa = \frac{1}{d}$ is the local curvature. Using the constitutive relationships (11) and (4) results in two equations representing the strain:

$$\kappa z = \frac{1}{Y_p} T_1 + d_{13} E_3, \tag{22}$$

$$\kappa z = \frac{1}{Y_S} T_1. \tag{23}$$

The resulting moments are obtained by multiplying by $z$ and integrating over the cross-section (in this case of a simplified plate the thickness instead of cross-section is used)

$$\int_z Y_p \kappa z^2 \,\mathrm{d}z = \int_z T_1 z \,\mathrm{d}z + \int_z d_{13} Y_p E_3 z \,\mathrm{d}z, \tag{24}$$

$$\int_z Y_s \kappa z^2 \,\mathrm{d}z = \int_z T_1 z \,\mathrm{d}z. \tag{25}$$

To better understand what the individual integrals mean, I will now represent them and describe their role in the problem. The first one is

$$M_s = -\int_z Y_s \kappa z^2 \,\mathrm{d}z, \tag{26}$$

a moment resulting from bending stiffness of the substrate. It can be clearly seen that the higher the Young's modulus of the substrate material is the more stiff is the layer. The stiffness also increases with the cross-section area.

The same applies for the piezoelectric layer (its mechanical part)

$$M_{pm} = -\int_z Y_p \kappa z^2 \,\mathrm{d}z. \tag{27}$$

The electrical part creates a bending moment (which acts against the two moments above) caused by an applied voltage across the piezoelectric layer

$$M_{pe} = \int_z d_{13} Y_1^E E_3 z \,\mathrm{d}z. \tag{28}$$

The reason for not using the Youn's modulus $Y_p$ is the fact that the piezo-induced moment comes from the active part of the MFC layer (ODKAZZZ).

Another moment can be added if there is external force acting on the plate. The associated moment is denoted $M_e$.

Assuming perfect bonding between the layers the moment equilibrium equation is

$$M_s + M_{pm} + M_{pe} + M_e = 0. \tag{29}$$

The curvature $\kappa$ is constant along $z$ (thanks to the aforementioned Euler-Bernoulli assumption) so it can be taken out of the integral. Rewriting (29) I get

$$\kappa C = \mathcal{M}_{pe} V, \tag{30}$$

where

$$C = \frac{EI}{w}. \tag{31}$$

The $EI$ is a product of second moment of inertia and Young's modulus. It represents bending stiffness of the beam (sometimes called flexural rigidity). $EI$ is used throughout the literature, but here with $w$ constant along the thickness $C$ is used for simplicity. The $C$ is in my case

$$C = \frac{1}{3}\left(Y_p\left((h_p - h_n)^3 + h_n^3\right) + Y_s\left((h_s + h_p - h_n)^3 - (h_p - h_n)^3\right)\right). \tag{32}$$

Table 6.1 shows the values of $EI$ and $C$ for the monomorph cantilever plate.

| Parameter [unit] | Value |
|---|---|
| $h_n$ [$\mu$m] | 675 |
| $EI$ [N·m$^2$] | 0.3982 |
| $C$ [N·m] | 6.3208 |

**Table 3.2.** The computed values of $h_n$, $EI$ and $C$.

The $\mathcal{M}_{pe}$ represents the piezoelectric induced moment per unit Volt. The moment is the actuator's/controller's input to the system. It is

$$\mathcal{M}_{pe} = d_{13} Y_1^E \frac{2h_n - h_p}{2}. \tag{33}$$

For small displacements (angles) the angle $\varphi$ can be approximated as

$$\varphi = \frac{\partial u_3}{\partial x}, \tag{34}$$

so that the displacement in the $x$-direction $u_1$ can be rewritten to

$$u_1 = \varphi z = \frac{\partial u_3}{\partial x} z. \tag{35}$$

Differentiating (21) I get $\kappa = \frac{\partial S_1}{\partial z}$ and with the use of (3) I can eventually rewrite equation (30) to

$$\frac{\partial^2 u_3}{\partial x^2} = \frac{\mathcal{M}_{pe}}{EI} V. \tag{36}$$

The equation (30) is in differential form. The transverse displacement $u_3$ can be obtained by integrating. Here it is where the piezoelectric layer length comes into the problem. Integrating twice over the length I get different results for different setups (boundary conditions). In case of more piezoelectric patches bonded to the beam, individual piezo-induced bending moments will be counted in by the integration. The integration constants are evaluated by incorporating the boundary conditions.

### 3.2.1 Solution to a monomorph cantilever

There are two boundary conditions for the cantilever in figure 3.4:

$$u_3(0) = 0, \tag{37}$$

$$\frac{\partial u_3(0)}{\partial x} = 0. \tag{38}$$

The (37) stands for the left end being fixed in position and the second equation (38) for the same end being fixed in rotation. The total displacement $u_3$ (with no external forces applied) is then

$$u_3(x) = \frac{\mathcal{M}_{pe}}{2EI} V x^2. \tag{39}$$

Below is a table of deflections of the tip for various voltages supplied to the piezoelectric layer. The displacements were calculated for $u_3(0.09)$ for the point I measured using an experimental setup. It will be compared to the measured data.

| Voltage $V$ [V] | 10 | 50 | 100 | 200 | 300 |
|---|---|---|---|---|---|
| Tip displ. $u_3$ [$\mu$m] | -41 | -205 | -409 | -818 | -1227 |

**Table 3.3.** Tip displacement of the cantilever.

The bending curve for $V = 200\,\mathrm{V}$ is plotted in 6.3. I included it to show the parabolic shape defined by (39).

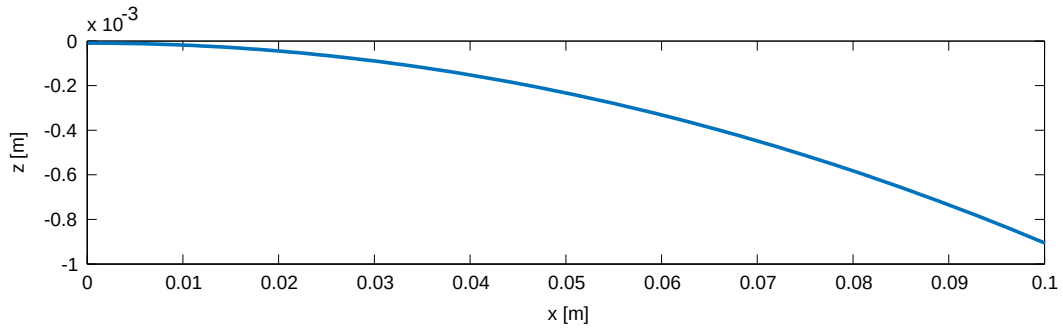


**Figure 3.6.** Parabolic deflection of the monomorph plate for $V = 200\,\mathrm{V}$.

### 3.2.2 Cantilever with a discontinuous voltage across its length

Let me now model a situation with either more piezoelectric patches of the same type (except the polarization) bonded to a cantilever or one piezoelectric layer with more electrodes. Two cases will be modeled, a case with 2 patches/electrodes and a case with 3 electrodes (figure 3.8).

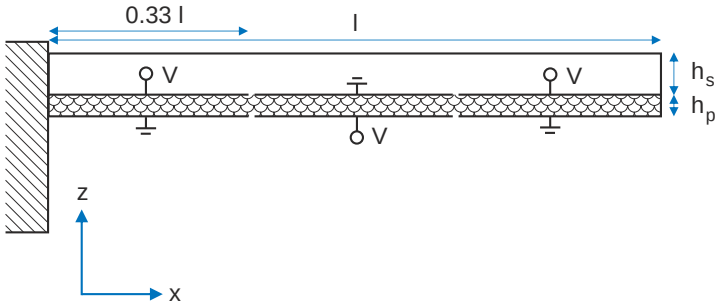


**Figure 3.7.** A cantilever with three electrodes.

General method for solving such discontinuities across the length of the cantilever is to integrate (36) and solve it by handling the integrals over individual subdomains (piezoelectric patches). Doing so I am able to obtain a solution for the fixed-free case. The same can be done for other boundary conditions.

The discontinuous voltage $v$ is in the form

$$v = \begin{cases} V & \text{if } x \leq \frac{l}{2}; \\ -V & \text{if } x > \frac{l}{2} \end{cases} \tag{40}$$

for the first case and

$$v = \begin{cases} V & \text{if } x \leq \frac{l}{3}; \\ -V & \text{if } \frac{l}{3} < x \leq \frac{2l}{3}; \\ V & \text{if } x > \frac{2l}{3}. \end{cases} \tag{41}$$

for the case with three piezoelectric patches. The analytical solution is

$$u_3 = \begin{cases} \eta V x^2 & \text{if } x \leq \frac{l}{2}; \\ \eta V (lx - \frac{x^2}{2} - \frac{l^2}{4}) & \text{if } x > \frac{l}{2} \end{cases} \tag{42}$$

for a case with two electrodes/patches.

For three electrodes it is

$$u_3 = \begin{cases} \eta V x^2 & \text{if } x \leq \frac{l}{3}; \\ \eta V(\frac{2l}{3}x - \frac{x^2}{2} - \frac{l^2}{9}) & \text{if } \frac{l}{3} < x \leq \frac{2l}{3}; \\ \eta V(\frac{x^2}{2} - \frac{2l}{3}x + \frac{l^2}{3}) & \text{if } x > \frac{2l}{3}. \end{cases} \tag{43}$$

where $\eta$ was substituted for

$$\eta = \frac{\mathcal{M}_{pe}}{2EI}. \tag{44}$$

Below (figure 3.8) is a plot of bending curves for both the cases (42) and (43).

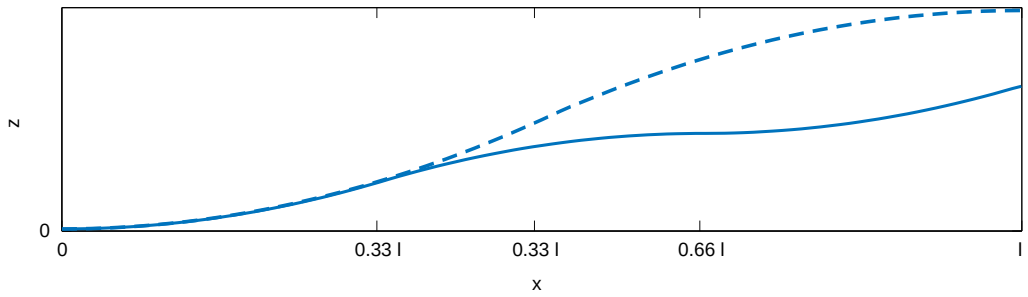


**Figure 3.8.** Deflection resulting from two (dashed line) and three electrodes (solid).

## 3.3 Dynamic analysis

Dynamic behavior of the plate will be analyzed in this section. The study is general and can be used not only in active and adaptive optics. Vibration analysis is very popular nowadays as it is possible to harvest energy from piezoelectric patches. And if tuned properly, the system can be optimized to maximize the energy harvested.

It is good to understand equations that approximate the motion. I will now do a short analysis of them. The linear part of the dynamics is in the form of the Euler-Bernoulli equation for a one-dimensional case (beam) [14]

$$\frac{\partial^2}{\partial x^2}\left(M(x,t)\right) + \rho A(x)\frac{\partial^2 u_3(x,t)}{\partial t^2} = f_e(x,t), \tag{45}$$

which is actually an extended (but undamped) version of (36) with inertia included. The external forces per unit length are denoted $f_e(t,r)$, inertial force of the plate is

$$F_I = \rho A\frac{\partial^2 u_3(x,t)}{\partial t^2}, \tag{46}$$

where $\rho$ is density of the beam and $A$ is its cross-sectional area, which can, in general, depend on $x$. The bending moment is the same as for the static analysis:

$$M = EI\frac{\partial^2 u_3(x,t)}{\partial x^2}. \tag{47}$$

I can now rewrite (45) with (47), for a constant flexural rigidity $EI$ I get

$$EI\frac{\partial^4 u_3(x,t)}{\partial x^4} + \rho A(x)\frac{\partial^2 u_3(x,t)}{\partial t^2} = f_e(x,t). \tag{48}$$

Now, after the short introduction to the linear part of the dynamics, a solution to it shall be found. The solution is sought in a separated form [13]:

$$u_3(x,t) = X(x)\phi(t) = X(x)\,\phi_0\,e^{j\omega t}. \tag{49}$$

### 3.3.1 Spatial response

I will start with a spatial response of the one-dimensional case. By plugging equation (49) back into (48) and dividing it by $EI$ I get

$$\frac{\partial^4 X}{\partial x^4} - k^4 X = 0, \tag{50}$$

which is a standard eigenvalue problem which is to be solved for $k$, where $k^4$ is

$$k^4 = \frac{\rho A\omega^2}{EI}. \tag{51}$$

A Laplace transform of (50)

$$\mathcal{L}\left\{\frac{\partial^4 X}{\partial x^4}\right\} - \mathcal{L}\left\{k^4 X\right\} = 0. \tag{52}$$

yields a solution in a spatial frequency domain

$$X(s) = \frac{1}{s^4 - k^4}\left(s^3X(0) + s^2X'(0) + sX''(0) + X'''(0)\right). \tag{53}$$

A solution in spatial coordinate $x$ would be understood much better and can be gotten as a inverse Laplace transform of (53). The resulting function is

$$X(x) = X(0)\, a(kx) + \frac{X'(0)}{k}\, b(kx) + \frac{X''(0)}{k^2}\, c(kx) + \frac{X'''(0)}{k^3}\, d(kx), \tag{54}$$

where the functions $a, b, c, d$ are so-called *Rayleigh shape functions*

$$a(kx) = \frac{1}{2}\left(\cos(kx) + \cosh(kx)\right),$$
$$b(kx) = \frac{1}{2}\left(\sin(kx) + \sinh(kx)\right),$$
$$c(kx) = \frac{1}{2}\left(-\cos(kx) + \cosh(kx)\right),$$
$$d(kx) = \frac{1}{2}\left(-\sin(kx) + \sinh(kx)\right).$$

Let me now incorporate the boundary conditions. Four of them are needed to be able to solve the fourth-order PDE. For the fixed-free case (figure 3.4) they are

$$\begin{aligned} X(0) &= 0, & X''(l) &= 0, \\ X'(0) &= 0, & X'''(l) &= 0. \end{aligned}$$

It is now obvious that the conditions have to be satisfied by incorporating them into the solution (54). I need to differentiate the equation to be able to use all the boundary conditions. After properly differentiating the equation and incorporating the first two boundary conditions I get $X(0) = 0$ and $X'(0) = 0$, which means that the boundary conditions are satisfied by the geometry of the shape functions itself.

The other two boundary conditions yield a set of equations

$$\begin{pmatrix} a(kl) & \frac{b(kl)}{k} \\ kd(kl) & a(kl) \end{pmatrix} \begin{pmatrix} X''(0) \\ X'''(0) \end{pmatrix} = \begin{pmatrix} 0 \\ 0 \end{pmatrix}. \tag{55}$$

The values $X''(0)$ and $X'''(0)$ represent a force and moment at $x = 0$ and must not be zero (fixed end at $x = 0$). So a non-trivial solution to (55) is sought, which means that the determinant of (55) has to be equal to zero. This condition results in a so-called *characteristic equation*. For the fixed-free beam (cantilever) it is

$$\cos(kl)\cosh(kl) + 1 = 0. \tag{56}$$

This transcendental equation needs to be solved numerically. The first 5 solutions to it are listed in table 3.4. The corresponding natural frequencies will be discussed later in section 3.3.2.

| Mode $n$ | 1 | 2 | 3 | 4 | 5 |
|---|---|---|---|---|---|
| $k_n l$ | 1.8751 | 4.6941 | 7.8548 | 10.9955 | 14.1372 |

**Table 3.4.** A numerical solution to the characteristic equation (56).

I can now rewrite the general solution (54) to the one of an $n$-th mode, a use of the boundary conditions reduces it to

$$X_n(x) = \frac{1}{k_n^2} X_n''(0) \left( c(k_n x) + \frac{1}{k_n} \frac{X_n'''(0)}{X_n''(0)} d(k_n x) \right). \tag{57}$$

From (55) the fraction $\frac{X_n'''(0)}{X_n''(0)}$ can be expressed and substituted in (58) so that I obtain the final solution of the $n$-th mode's spatial response

$$X_n(x) = \frac{1}{k_n^2} X_n''(0) \left( c(k_n x) - \frac{a(k_n l)}{b(k_n l)} d(k_n x) \right). \tag{58}$$

Normalized modes defining the shape are represented by the term in the bracket. The value preceding it is arbitrary and only scales them. The first five normalized modes are plotted in figure 3.9.

The superposition of modes

$$u_3(x,t) = \sum_{n=1}^{\infty} X_n(x)\phi_n(t) \tag{59}$$

represents the spacial response of a cantilever.

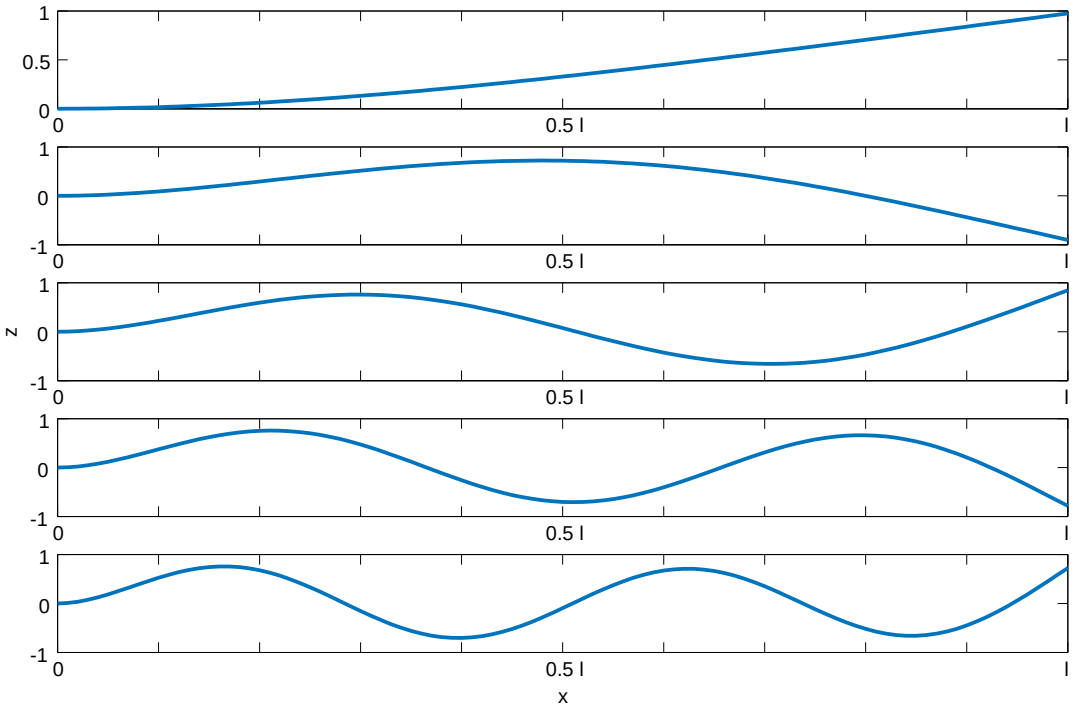


**Figure 3.9.** First 5 normalized spatial modes of a transverse vibration of a one-dimensional structure.

### 3.3.2 Time response

One might wonder what the time response of individual modes is. It has been represented by the $\phi_n(t)$ in equation (59) till now. The separation of time and space helps solve it separately. Plugging the solution (59) into the Euler-Bernoulli equation (48), integrating it to get rid of the differential dimensionless form yields

$$EI\sum_{n=1}^{\infty}\int_0^l \frac{d^4X_n}{dx^4}\phi_n\,dx + \rho A\sum_{n=1}^{\infty}\int_0^l \frac{d^2\phi_n}{dt^2}X_n\,dx = \int_0^l f_e(x,t)\,dx, \tag{60}$$

which is just what is expected — i. e. the second derivative in time in the PDE yields a second-order model (undamped in this case) in the form (a detailed derivation can be found in [13])

$$\ddot{\phi}_n + \omega_n^2\phi_n = \frac{\int_0^l f_e X_n\,dx}{\rho A\int_0^l X_n^2\,dx}. \tag{61}$$

Let me now exclude the external forces to obtain a solution called the *free vibration*:

$$\ddot{\phi}_n + \omega_n^2\phi_n = 0. \tag{62}$$

The spatial and time response are naturally interconnected. Each spatial mode has its own natural frequency characterizing its time response. The interconnection in the model is provided by a mathematical description of its relationship, the dispersion relation (51). The natural frequencies can be obtained from

$$\omega = \sqrt{\frac{EI}{\rho A}}k^2. \tag{63}$$

| Mode $n$ | 1 | 2 | 3 | 4 | 5 |
|---|---|---|---|---|---|
| $k_n$ [m$^{-1}$] | 19.63 | 49.15 | 82.25 | 115.14 | 148.03 |
| $\omega_n$ [rad·s$^{-1}$] | 551 | 3452 | 9667 | 18945 | 31314 |
| $f_n$ [Hz] | 88 | 549 | 1539 | 3015 | 4984 |

**Table 3.5.** First five solutions to (63) (modes of the cantilever).

The solutions to (63) are shown in table 3.5. In order to evaluate it I used table 3.4, $EI$ value from table 6.1 and $\rho$ from (2).

### 3.3.3 Two-dimensional vibrations

The analytical model presented above is not suitable for analyzing two-dimensional cases. It might be possible to obtain a model, but sometimes it is not possible to solve the eigenvalue problem, so a more approximating theory comes handy. One such an approximation is the *Rayleigh-Ritz* method. The shape function $w(x,y,t)$ is approximated by a linear combination of $n$ *admissible functions* $\Psi(x,y)$

$$w(x,y,t) = \boldsymbol{\Psi}(x,y)\,\mathbf{q}(t). \tag{64}$$

It is a special set of functions (usually polynomials) which are selected to satisfy geometry of the system (i. e. boundary conditions). Here $\mathbf{q}(t)$ is a time-only dependent

vector for which we solve the problem. The Lagrange approach is used to formulate the dynamics of the system which eventually shrinks to a standard form

$$\mathbf{M}\ddot{\mathbf{q}} + \mathbf{K}\dot{\mathbf{q}} = \mathbf{F}, \tag{65}$$

where $\mathbf{M}$ is the system's mass matrix, $\mathbf{K}$ is the stiffness matrix and $\mathbf{F}$ is the effect of external forces. Solving the eigenvalue problem ($\mathbf{F} = \mathbf{0}$) of the equation above yields the desired eigenvalues and corresponding eigenvectors.

There are other methods for evaluating the frequencies and modes for plate vibrations. The choice of such a method depends on the boundary conditions as the methods are only for some of the 21 combinations (4 edges, each can be free, simply supported or clamped). The whole plate theory including various methods is covered in [15].

A great book called *Formulas for natural frequency and mode shape* [16] offer engineers numerical results for the first 6 plate modes for every of the 21 combinations. Not only rectangular plates are covered by this book — hundreds of different shapes and kinds of plates, shells and trusses are covered too. I used [16] to calculate the natural frequencies for my case. I picked a rectangular ratio $\frac{l}{w} = 1.5$ which is the closest value listed. The Poisson's ratio used is 0.3. I used the frequency of the first mode obtained in section 3.3.2 as a reference. The resulting mode shapes and frequencies $f_n = \frac{\omega_n}{2\pi}$ are listed in table 3.6.

| Mode $n$ | (1, 1) | (1, 2) | (2, 1) | (2, 2) | (1, 3) | (3, 1) |
|---|---|---|---|---|---|---|
| $f_n$ [Hz] | 88 | 296 | 547 | 999 | 1364 | 1569 |

**Table 3.6.** First six numerical solutions (modes) for $f_n$.

# Chapter 4
# Finite element models

The finite element method (FEM) was used as a second tool for modeling the plate. FEM is a very popular way of modeling flexible structure. Many modules supporting the piezoelectric effect can be found on the market. I used Structural Mechanics and MEMs module[1]) as an extension to Comsol Multiphysics.

The initial idea was to use Comsol as a tool for exporting modal matrices, that could be used to produce a modal state-space model useful for control. After finding several bugs in Comsol's software (the part that had bugs is an additional software called *LiveLink for MATLAB*), I decided to give up and focus on things that can be done within the Comsol Multiphysics itself. Static simulations will serve for validating displacement and shape, dynamic simulations will yield mode shapes and the corresponding natural frequencies.

I will first present the basics of FEM for the electromechanical case in section 4.1, and then use it to model the plate by including the dynamics 4.3 or omitting it 4.2.

## 4.1 MDOF formulation

The method is based on using a finite number elements. The plate is simply divided into elements (points), carefully chosen to represent motion (or other physical phenomenon) of the plate. I would have an infinite number of points to model every detail. Working with infinity can be done symbolically, but it is not suitable for numerical algorithms run on PCs. Therefore, a carefully chosen finite set of points is used instead. It is usually defined as a *mesh*, which prescribes the points locations (figure 4.2).

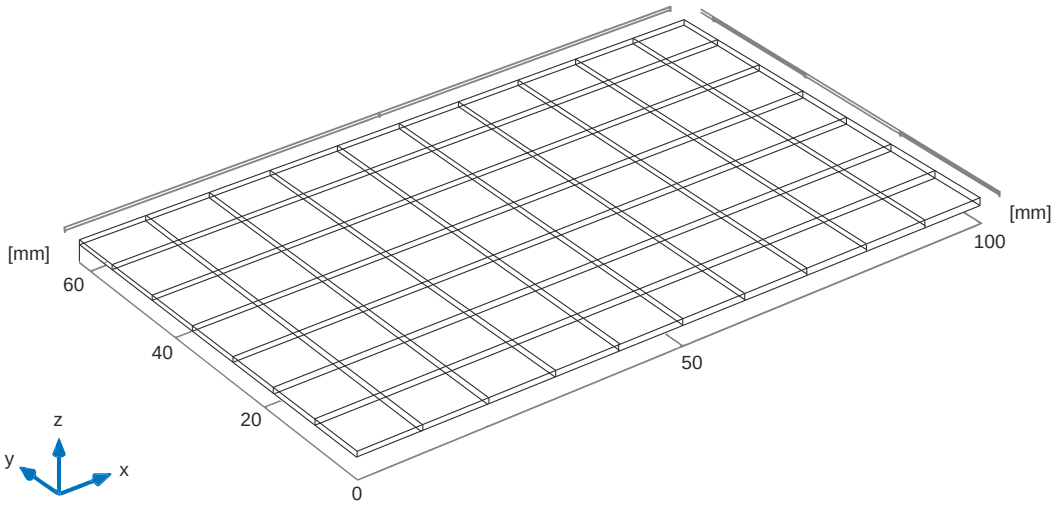


**Figure 4.1.** Mapped-swept mesh of the cantilever plate.

[1]) `http://www.comsol.com/products/mems/`

Having a set of points I can find its equation of motion either by Newton's or Lagrange's approach. The dynamic behavior of one point is described by a second-order differential equation in time

$$m\ddot{x} + b\dot{x} + kx = F_e, \tag{1}$$

which can be rewritten using a state vector $\mathbf{q} = \begin{pmatrix} x \\ \dot{x} \end{pmatrix}$ to obtain a state-space model

$$\dot{\mathbf{q}} = \mathbf{A}\mathbf{q} + \mathbf{B}F_e. \tag{2}$$

The $F_e$ is an external force acting on the point, $m$ is the inertance (mass) of the point, $k$ its compliance (stiffness) and $b$ its damping. Equations (1) and (2) express dynamic behavior of a damped single degree of freedom (1DOF) problem. To cover all the dynamics, two state variables for one DOF are needed.

A set of more points can be described the same way. The number of states is twice the number of degrees of freedom, which equals the number of points. The governing matrix equation is:

$$\mathbf{M_x}\ddot{\mathbf{x}} + \mathbf{B_x}\dot{\mathbf{x}} + \mathbf{K_x}\mathbf{x} = \mathbf{F_e}. \tag{3}$$

It expresses the same as (1) and again the $\mathbf{M_x}, \mathbf{K_x}, \mathbf{B_x}$ is the mass, stiffness and damping matrix respectively. The matrix $\mathbf{F_e}$ is composed of external forces acting on individual points and vector $\mathbf{x}$ is composed of all points included in the analysis.

The electrical part of the system is often modeled statically. The reason for it is the fact that the mechanical response is much slower than that of the electrical part. The governing equation for MDOF (multi DOF) electrostatics is

$$\mathbf{K_\Phi}\mathbf{\Phi} = \mathbf{Q_e}, \tag{4}$$

where $\mathbf{\Phi}$ is an electric potential, $\mathbf{K_\Phi}$ is the matrix of electrical compliance (i. e. capacitance), and $\mathbf{Q_e}$ is a matrix of electric charges brought to the electrodes.

Including the electromechanical coupling effects means adding coupling terms to both the equations (3), (4) so that eventually I get

$$\begin{pmatrix} \mathbf{M_x} & \mathbf{0} \\ \mathbf{0} & \mathbf{0} \end{pmatrix} \begin{pmatrix} \ddot{\mathbf{x}} \\ \ddot{\mathbf{\Phi}} \end{pmatrix} + \begin{pmatrix} \mathbf{B_x} & \mathbf{0} \\ \mathbf{0} & \mathbf{0} \end{pmatrix} \begin{pmatrix} \dot{\mathbf{x}} \\ \dot{\mathbf{\Phi}} \end{pmatrix} + \begin{pmatrix} \mathbf{K_x} & \mathbf{K_{x\Phi}} \\ \mathbf{K_{x\Phi}} & \mathbf{K_\Phi} \end{pmatrix} \begin{pmatrix} \mathbf{x} \\ \mathbf{\Phi} \end{pmatrix} = \begin{pmatrix} \mathbf{F_e} \\ \mathbf{Q_e} \end{pmatrix}. \tag{5}$$

An ideal source is assumed as there is no damping in (5) for the electrical part.

## 4.2 Static FEM

The static finite element analysis reduces the equation (5) so that only potentials are analyzed. It is the displacement in the mechanical domain and electric potential for the electrical domain. The resulting equations for static FEM are:

$$\begin{pmatrix} \mathbf{K_x} & \mathbf{K_{x\Phi}} \\ \mathbf{K_{x\Phi}} & \mathbf{K_\Phi} \end{pmatrix} \begin{pmatrix} \mathbf{x} \\ \mathbf{\Phi} \end{pmatrix} = \begin{pmatrix} \mathbf{F_e} \\ \mathbf{Q_e} \end{pmatrix}. \tag{6}$$

A simulation I performed for a single piezoelectric patch yielded the same parabolic shape as the one described by equation (39) in section 3.2.1. A visualization of the 2D model is shown in figure 4.2. The tip displacement obtained from the model for an electrodes voltage $V = 10\,\mathrm{V}$ was -41 $\mu m$.

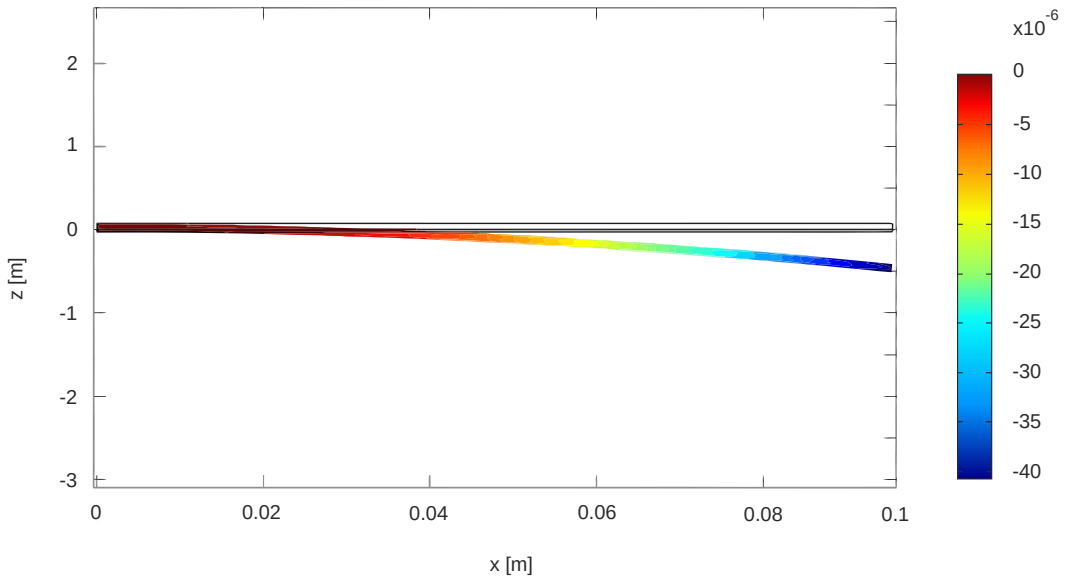


**Figure 4.2.** Simplified plate (cantilever) deflection using a 2D FEM model ($V = 10\,\mathrm{V}$).

Table 4.1 shows tip displacements obtained for various input voltages. The model is fitted with material properties from table 2.2. The supplied voltage was scaled by a constant due to the fact that the thickness of the active layer is much thinner than the actual MFC actuator (section 2.2).

| Voltage $V$ [V] | 10 | 50 | 100 | 200 | 300 |
|---|---|---|---|---|---|
| Tip displ. $u_3$ [$\mu$m] | -41 | -203 | -406 | -813 | -1220 |

**Table 4.1.** Tip displacement of the cantilever using the 2D FEM model.

## 4.3 Dynamic FEM

For dynamic analysis I will be using equation (5) derived above, which when converted to the state-space form is actually a set of differential-algebraic equations (DAEs), an expanded form of (2)

$$\mathbf{E_q}\dot{\mathbf{q}} = \mathbf{A_q}\mathbf{q} + \mathbf{B_q}\mathbf{F_e}. \tag{7}$$

The matrix $\mathbf{E_q}$ is usually singular. It is useful to note that there are algebraic equations coming from the static description of the electrical part. The reason is that not every solver is capable of solving DAEs directly (due to the mentioned singularity).

The form (5) is a so-called nodal form of the model. It directly expresses its behavior in terms of the plate's inertia, stiffness and optionally damping.

The nodal form can be converted into the aforementioned modal form so that the motion of the flexible structure is expressed as a combination of different modes (shapes) rather than different points. The conversion is sometimes called a *modal decomposition*. The transformation from nodal to modal coordinates is found using the general solution to (5). I already used the general solution in section 3.3, equation (49). Plugging the solution into the undamped free vibration case of (3)

$$\mathbf{M_x}\ddot{\mathbf{x}} + \mathbf{K_x}\mathbf{x} = \mathbf{0} \tag{8}$$

yields

$$(\mathbf{K_x} - \omega^2\mathbf{M_x})X(\mathbf{x})\phi_0 e^{j\omega t} = 0. \tag{9}$$

A nontrivial solution is sought in this case. To find one for the homogeneous set of equations (9) the determinant of it must be equal to zero:

$$|\mathbf{K_x} - \omega^2\mathbf{M_x}| = 0. \tag{10}$$

The equation above has a set of solutions denoted $\omega_n$, where $n = 1, 2, ..$ up to the number of degrees of freedom of the system. In case of a flexible structure which has infinitely many degrees of freedom, an infinite set of solutions exists. The $\omega_n$ are called natural frequencies (or eigenfrequencies) and the corresponding solutions $X_n = X_n(\mathbf{x})$ for each one of them

$$(\mathbf{K_x} - \omega_n^2\mathbf{M_x})X_n\phi_0 e^{j\omega_n t} = 0. \tag{11}$$

are called the mode shapes (eigenvectors). It can be shown that the eigenvectors are orthogonal with respect to the stiffness and mass matrices [17].

The resulting transformation between the nodal ($\mathbf{x}$) and modal ($\mathbf{z}$) coordinates is

$$\mathbf{x} = \mathbf{Z}\mathbf{z}, \tag{12}$$

where $\mathbf{Z} = (X_1, X_2, ..)$ is a matrix of mode shapes and $\mathbf{z}$ their corresponding amplitudes. The transformation results in the expected second-order model described by mode shapes with amplitudes varying (oscillating) in time. For the undamped case of free vibration (8) it is

$$\mathbf{M_x}\mathbf{Z}\ddot{\mathbf{z}} + \mathbf{K_x}\mathbf{Z}\mathbf{z} = \mathbf{0}. \tag{13}$$

The damped case with external loads included is then

$$\mathbf{M_x}\mathbf{Z}\ddot{\mathbf{z}} + \mathbf{B_x}\mathbf{Z}\dot{\mathbf{z}} + \mathbf{K_x}\mathbf{Z}\mathbf{z} = \mathbf{F_e}. \tag{14}$$

### 4.3.1 Input-output model

It can be shown [14], [18] that thanks to the orthogonality, the set of equations (13) can be transformed into an input-output model. A one-dimensional case for the transverse displacement $u_3 = u_3(x,t)$ might be assumed to have a separate solution as (49) in section 3.3. The time-frequency Laplace transform of it, which I will use later, is

$$U_3(x,s) = \sum_{n=1}^{\infty} X_n(x)\Phi_n(s). \tag{15}$$

The solution in time $\phi_n(t)$ for an undamped case can be rewritten using the orthogonality conditions [14] so that it matches (61) from section 3.3.2:

$$\ddot{\phi}_n + \omega_n^2 \phi_n = Q_n(t), \tag{16}$$

the variable $Q_n = \int_x X_n(x) f(x,t)\, dx$ can often be decomposed to

$$Q_n(t) = F_n u(t). \tag{17}$$

The Laplace transform of (16)

$$s^2\Phi_n(s) + \omega_n^2\Phi_n(s) = Q_n(s), \tag{18}$$

and use of a Laplace transformed relation (17) result in a transfer function for one single ($n$-th) mode

$$G_n(s,x) = \frac{\Phi_n(s)}{U(s)} = \frac{X_n F_n}{s^2 + \omega_n^2}. \tag{19}$$

The complete solution is then obtained by including all the terms as in (15)

$$G(s,x) = \sum_{n=1}^{\infty} \frac{X_n F_n}{s^2 + \omega_n^2}. \tag{20}$$

The transfer function is an idealized undamped case. A damping can be added to the denominator, it would be denoted in the standard notation $\zeta_n$ as a damping ratio for the $n$-th mode. The upper limit ideally goes to infinity for a flexible problem with infinitely many degrees of freedom. For a finite number of points in the nodal coordinates (which is an approximation of the real problem) a finite number of modes is obtained. And the transfer function sum's upper limit is finite. A finite element model is actually a set of the most influencing shape modes.

The transfer function (20) represents parallel (decoupled) connection of second-order systems (each with its own mode shape and natural frequency given by the dispersion relation (51)). The more subsystems the better the accuracy of the model as a whole. The amplitudes of the mode shapes at higher frequencies are attenuated though, so it is not a big error to cut them off, keeping only the modes that have the largest displacement amplitudes.

### 4.3.2 Simulation

The simplified two-dimensional case has $n$ modes with frequencies $f_n$. I obtained exact values using the 2D FEM model already used in figure (6). The first 5 mode shapes are those plotted in figure 3.9. The corresponding natural frequencies calculated by Comsol are listed in table 4.2.

| Mode $n$ | 1 | 2 | 3 | 4 | 5 |
|---|---|---|---|---|---|
| $f_n$ [Hz] | 86 | 536 | 1501 | 2937 | 4848 |

**Table 4.2.** First five modes and corresponding frequencies of the 2D FEM model.

I also created a 3D model using the dimensions from table 2.1 and other required parameters from table 2.2. In this case full material matrices were needed. These were hard to get as only some of the parameters can actually be measured or they are not really influencing simulations and/or experiments. So only a few parameters are listed in the manufacturers catalogs. I therefore assumed the piezoelectric layer to be of an orthotropic material, for which I only needed a few parameters that can be found in the available datasheets [10], [8]. The silicon wafer was modeled as an isotropic material, using two parameters only: its Young's modulus and Poisson's ratio.

Simulating in 3D, I was able to let Comsol evaluate eigenvalues $\omega_n$ of the plate. The first 9 modes marked in the $(m, n)$ fashion are plotted in figure 4.3. The number $m$ stands for a longitudinal mode (along the x-axis), whereas $n$ stands for perpendicular lateral modes (along the y-axis).

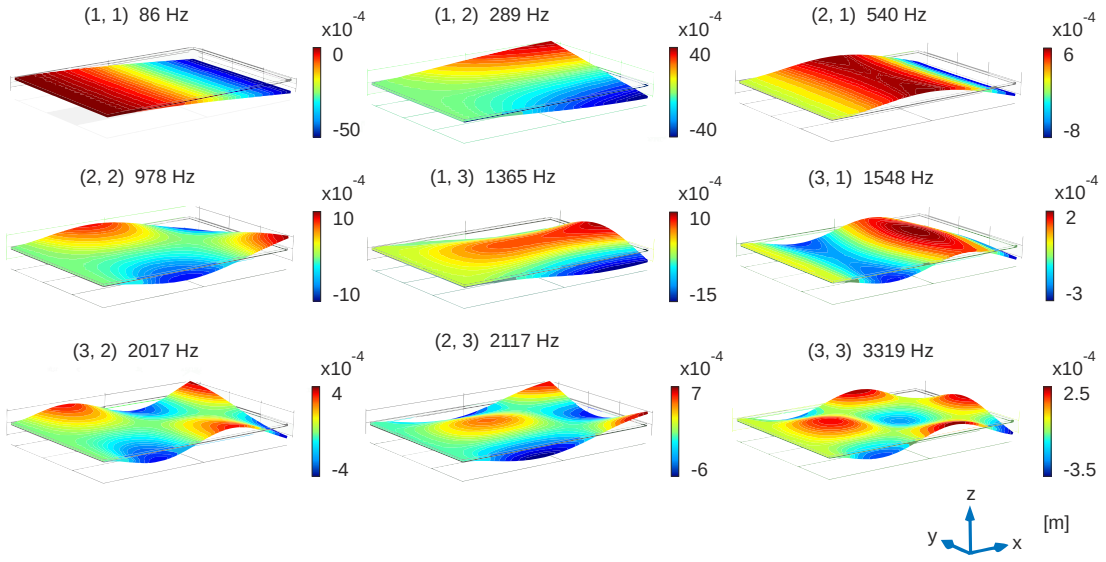


**Figure 4.3.** First 9 vibrational modes including the eigenfrequencies evaluated by Comsol (the (4, 1) mode at 3103 Hz is preceding the (3, 3) mode which is actually the 10th mode).

# Chapter 5
# Nonlinearities

The piezoelectric material with similar characteristics to PZT-5A used in the Smart Material's MFCs exhibits standard piezoelectric non-linearities such as hysteresis, depolarization and creep. Most of the non-linearities come from the fact that piezoceramics such as PZT are composed of ferroelectric domains, each of a uniform polarization. There is a close analogy with magnetic domains. I will briefly describe the piezoelectric nonlinearity, evaluate its consequences and decide whether or not to include such flaws in the model (sections 5.1, 5.2, 5.3).

Other nonlinearities come from the fact that the measurement and control setup itself is part of the system and it must be considered too. I will briefly go through it in sections 5.4 and 5.5.

All the nonlinearities come with the actuator and sensor. The plant itself (the bending cantilever plate) is assumed linear (models from chapters 3 and 4).

## 5.1 Depolarization

The ceramic piezoelectric devices are manufactured from must be *poled*. It is a process of aligning ferroelectric domains in one direction — a so called *poling direction*. The poling process is usually done by applying high electric fields (1-10 MV/m) during high temperatures. The polarized ceramic exhibits piezoelectric properties, whereas a non-poled ceramic does not, because individual arbitrarily polarized domains cancel out from the macroscopic point of view.

The poling voltage for the piezoelectric patch I analyzed (MFC-8557-P2) is just $V_{pol} = 450\,\mathrm{V}$, the operating voltage for the same piezoelectric patch is $V_{min} = -60\,\mathrm{V}$ and $V_{max} = 360\,\mathrm{V}$ (taken from [10]). The reason for this is the effect of depolarization. The poling voltage is low compared to the operating voltage so it is obvious that there is a vast influence between the electric field and the piezoelectric domains polarization. In other words the piezoceramic poles itself by the operating voltage. The effect of such a poling is not that large when keeping the voltage within the recommended operating region, but it still results in a phenomenon called hysteresis which will be described and modeled in section 5.3.

If I wanted to operate the piezoelectric patch out of the recommended range what would happen is that the material's polarization would suddenly switch by applying negative voltage. This depolarization effect results in a so-called *butterfly loop*, i. e. a voltage-strain (in my case voltage-displacement) plot. The piezo-overlain cantilever thus exhibits the same behavior and its butterfly loop I measured is shown in figure 6.8 in section 6.4. The sudden switch is followed by a phenomenon called *creep*.

## 5.2 Creep

Creep is a phenomenon which is caused by the nature of piezoelectric ceramics and its structure. The ferroelectric domains influence each other so when a change of polarization (change in applied voltage) is made a sudden change in strain or stress is observed,

but it keeps on going even if the input voltage does not change at all. Meaning that it takes time for the material to reach equilibrium. Time constants of the creep (which decreases logarithmically with time) can go up to 100 seconds. One could call this effect an inertia of piezoelectric polarization.

The creep effect can be seen in figure 6.8 and occurs after the sudden depolarization at roughly $\pm 200\,\mathrm{V}$.

This nonlinearity not really influences the cantilever in my case and I will thus not model it. The trend in modeling piezoelectric problems is not to include the creep. Several models exist though, some of them can be found in [19] and [20].

## 5.3 Hysteresis

The major non-linear phenomenon regarding piezoceramics is that they exhibit hysteresis. It is of the same cause as in 5.1 and 5.2. The difference though is the view. In this case it is a change in polarization influencing quality of the piezoelectric effect. By the word quality I mainly mean the coupling $d$ constant (matrix) which is not constant at all (it depends on the voltage, temperature and time). The time dependence is the mentioned creep and temperature dependence can be omitted. There is a small change in polarization even for the smallest change of the voltage. These changes result in better or worse quality of the piezoelectric effect which depends on whether I change the polarization in favor of $d$ or opposing to it.

Several models that come from the deep understanding can be found, e. g. a domain-wall model [21]. These models describe the domain wall switching in the material and are very precise. Its not useful for control purposes for its complexity though. The models great advantage is their outstanding accuracy resulting from the fact that they directly describe the underlying physics.

Another possibility to model hysteresis is just to "describe" its behavior. Meaning to describe it mathematically. Many descriptions exist, most of them are based on simple models of generalized relays often called *hysterons*. The models can be extended up to a infinite number of hysterons — in most cases a weighted parallel connection of these. Currently available descriptions include Preisach model, Prandtl-Ishlinskii model, Maxwell slip model, etc.

Other approaches come up with a totally different approach. They use the fact that there is small, or even no hysteresis in the charge–strain relationship. One might then control the charge instead of voltage as in [22] and [23].

### 5.3.1 Rate-dependence

Rate-dependence and independence is a phenomenon of the hysteresis changing shape with higher rate. The rate does not directly means frequency, but frequency is mostly used to measure the rate-dependence. The higher the rate the bigger the losses are in real actuators and the larger the hysteresis loop area (which represents the losses) is. Only idealized actuators can be assumed rate-independent or those that are restricted to operate within a narrow frequency band.

The hysteresis in my thesis is idealized, rate-independent. The reason is that I do not think the actuator would ever be used in the high frequency (hundreds of Hertz) band. It is not needed for the purpose of adaptive and active optics.

### 5.3.2 Prandtl-Ishlinskii model

The *Prandtl-Ishlinskii* (PI) model of hysteresis is one of the mathematical models using hysterons. It is a so-called *backlash* operator in this case, coming from the backslash of two gears. Its mathematical description according to [24] leads to

$$y(t) = \max\left\{x(t) - r, \min\left\{x(t) + r, y(t - T)\right\}\right\}, \tag{1}$$

where $y(t)$ is the output at time $t$, $x(t)$ is the input, $r$ is the magnitude of the backlash and $T$ is the sampling period. The initial value $y(0)$ must satisfy the equation, in my case it is $y(0) = 0$ for a zero cantilever tip displacement.

A weighted combination (parallel connection) of more backlashes

$$y(t) = \sum_{b=1}^{N} w_b \max\left\{x(t) - r_b, \min\left\{x(t) + r_b, y_b(t - T)\right\}\right\}, \tag{2}$$

where $N$ is their total number, $b$ represents the b-th backlash operator and $w_b$ its weight results in a shape of the hysteresis loop similar to that of the piezoceramics.

The model used for identification comes from [25] and I adopted it from Jiří Figura's concurrent thesis on modeling and control of the piezoelectric hysteresis [26]. The identification was done using 12 backlash operators whose parameters were found using the least squares method. The measured hysteresis (input voltage vs. output displacement) is on the left of figure 5.1, the identified model compared to the input is shown on the right. The hysteresis loops counterclockwise in this case.

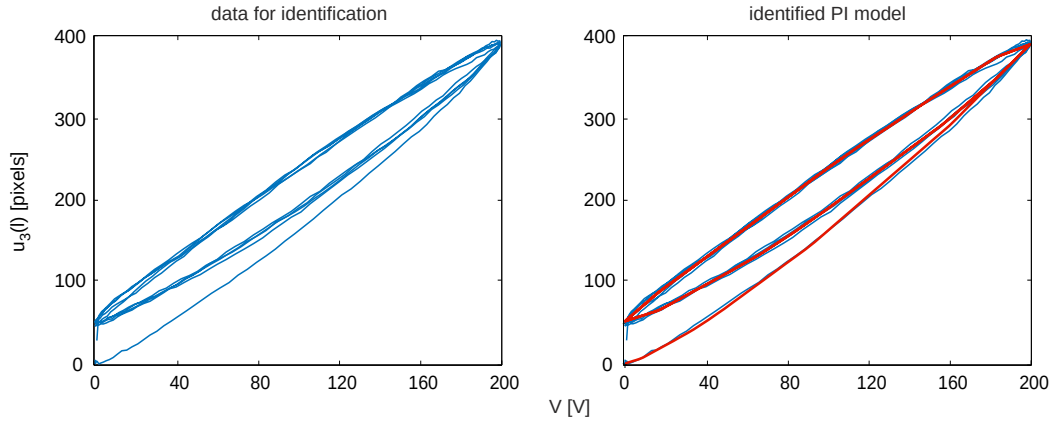


**Figure 5.1.** Measured input-output relation compared to the identified PI model's output.

## 5.4 Actuator amplifier

Another part of the actuator that has to be taken into account is the voltage amplifier. The very small (38 × 38 × 16 mm) amplifier EMCO G05 that I got with the project assignment amplifies voltage from 0–12 V to 0–500 V. The voltage amplification is almost linear with a small 40 V dead zone near zero. I found a much larger issue for the control purposes — the G05 not only amplifies the voltage it also amplifies current in the same ratio. Even though it is rated at 1.5 W the amplifier does deliver it only at full voltage (output voltage of 500 V and the corresponding current of 1 mA give 1.5 W). When the voltage to be amplified drops, so does the current (e. g. for 200 V its only

1 mA). The problem of charging of the piezoactuator, which is electrically represented by a capacitor, will be measured and discussed in section 6.5.

The same applies to the actual voltage source. If it has current limitation it should be set in a way it does not influence the system. The piezoactuator can be electrically described as a capacitor with capacitance $C$, the current $i(t)$ through the capacitor is

$$i(t) = C\frac{\mathrm{d}v}{\mathrm{d}t}. \tag{3}$$

A harmonic signal with a frequency $f$ and peak-to-peak voltage $V_pp$ in the form

$$v(t) = \frac{V_{pp}}{2}\cos(2\pi f t) \tag{4}$$

results in a current according to (3). The maximum (peak) current is thus

$$i_{max} = \pi f C V_{pp}. \tag{5}$$

Other notes regarding driving piezoelectric loads are for example in [27].

## 5.5 Sensor

The last nonlinearity to be discussed is the sensor part. The measurement setup in the way I built it is nonlinear. The nonlinearity comes from the geometry and includes trigonometric functions. The relation between the distance measured by the line camera and the real deflection of a point of the plate is

$$l_s = l_1 + l_2 = d_1\frac{\sin\beta}{\sin(\alpha-\beta)}\left(\sin(2\alpha) - \cos(2\alpha)\tan(2\beta)\right) + d_2\tan(2\beta). \tag{6}$$

The equation is derived according to figure 5.2. I chose the inclination angle $\alpha$ to be $\frac{\pi}{4}$ to maximally simplify the equation to

$$l_s = d_1\frac{\sin\beta}{\sin\left(\frac{\pi}{4}-\beta\right)} + d_2\tan(2\beta). \tag{7}$$

Including the assumption that the deflection is parabolic (section 3.2.1) doubles the slope of the dotted cantilever in figure 5.2, and so the angle $\zeta$. Assuming small deflections (angles $\beta$) for simplification and including the parabolic shape results in

$$l_s = d_1\frac{\beta}{\frac{\pi}{4}-\beta} + 4d_2\beta. \tag{8}$$

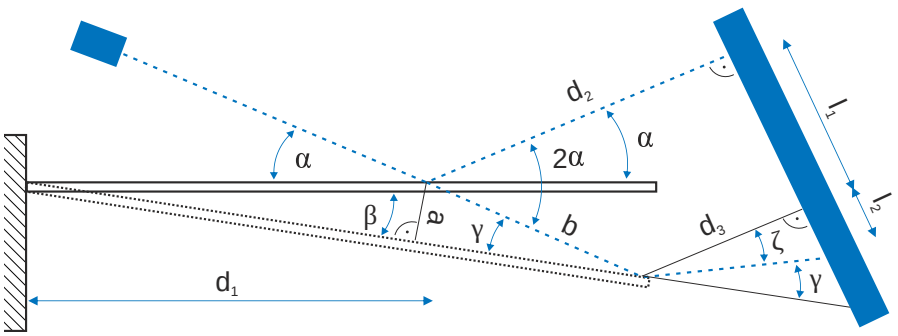


**Figure 5.2.** Measured input-output relation compared to the identified PI model's output.

# Chapter 6
# Measurements

The cantilevered plate was measured at one point using the optical setup in figure 5.2 using a laser beam reflected to a line CCD camera Thorlabs LC100. The LC100 has a single row of 2048 pixels, each 14 $\mu$m thick. The total displacement that can be measured is

$$2048 \times 14\,\mu\text{m} = 28.672\,\text{mm}.$$

The camera is able to deliver a stunning frame rate of 900 fps (internal trigger). In case an external trigger is used the frame rate drops to 450 fps. The LC100 is so sensitive that a current supplying the laser had to be set to minimum value and even though a total flood of charge occurred. I had to add several layers of paper sheets to cover the sensor and thus reduce its sensitivity. I finally ended up with a finely tuned CCD array (figure 6.1). To remove background noise I used a box covering the whole experiment so that no external light could disturb it.

The plot of pixel intensities in figure 6.1 shows that the laser beam is of no quality. A position of the intensity peak is used to determine the beam's position. I wrote a C script for this purpose as the supplied LC100 driver failed to work in MATLAB. Thorlabs fixed the issue later so I could use a 32-bit driver for MATLAB. It was still not fully functional, but I managed to implement it and use in Simulink to maintain better synchronization between the actuator and sensor.

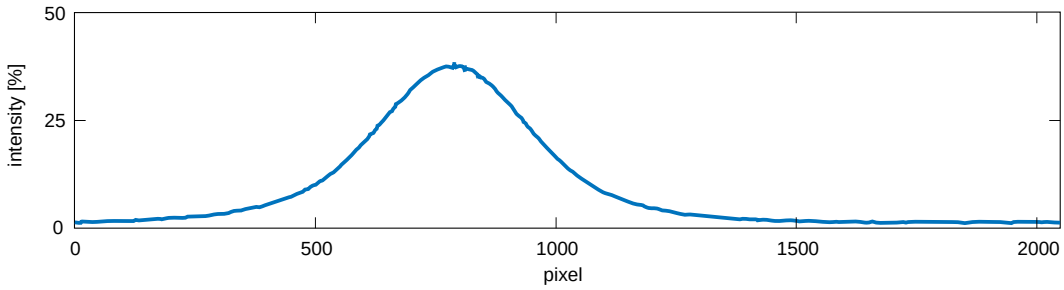


**Figure 6.1.** Light intensity measured on all of the LC100's pixels (integration time 1.05 ms).

For small deflections of the cantilever the measurements on the CCD camera can be assumed linear. It is not exactly linear though as the relation between the deflection of the plate and the laser beam is not linear. More on this can be found in section 5.5.

Two options were used to supply the actuator. The first one, with which I started the measurements, was a small 1.5W G05 from EMCO High Voltage[1]). This is a unit the project was assigned with. I found that it has certain limitations and should be used wisely (to be discussed in section 6.5). The limitations comes mainly from the fact that the amplifier itself has size of a matchbox. The second option for amplification

[1]) `http://www.emcohighvoltage.com/pdfs/gseries.pdf`

was a large laboratory linear amplifier EPA 104 from Piezo Systems[1]). This device is able to deliver ±200 V and a peak current of 200 mA. Its linearity is very good, much better than that of EMCO G05.

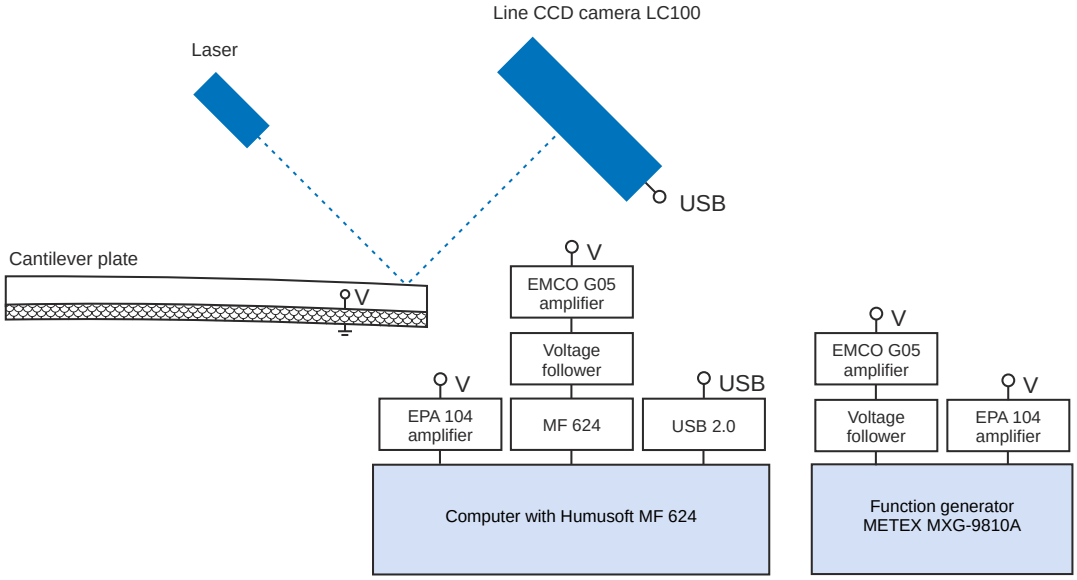


**Figure 6.2.** Instrument combinations used for the deflection measurements.

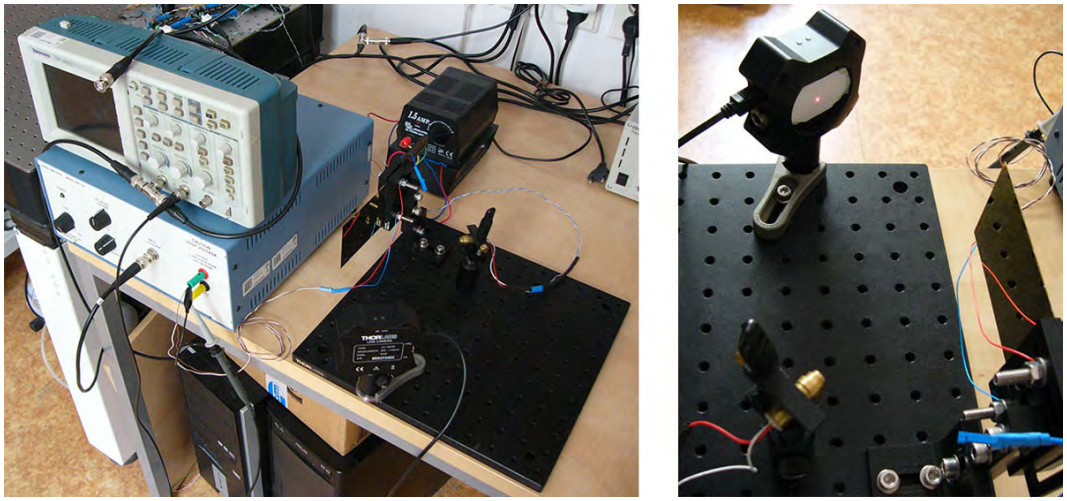

**Figure 6.3.** The measurement setup with EPA 104 amplifier connected to the piezoelectric patch (left image). A detailed view of the reflected laser beam (right).

The input signal was generated by a computer and outputted using a Humusoft MF 624 I/O[2]) card or by a function generator METEX MXG-9810A[3]). I used a voltage follower the amplifier in case of the EMCO amplifier due to its nonzero input resistance. Draining current from the MF 624 or the function generator would not be a good idea since their outputs are designed to make a perfect shape of the voltage function and not to be a source of current.

[1]) `http://www.piezo.com/prodelect1epa104.html`
[2]) `http://www.humusoft.cz/produkty/datacq/mf624/`
[3]) `http://www.tequipment.net/MetexMXG-9810A.html`

I used all four combinations of EPA 104, EMCO G05 and MF 624, METEX generator (figure 6.2). Due to a buggy LC100 driver for MATLAB the external mode in Real-Time Workshop in Simulink could not be used so I used the normal mode only. The normal mode was able to deliver a 10millisecond precision, but no better. That is why I also used the function generator. The measurements of faster signals were made using the program that I coded in C. I was then able to read output from the line camera at the full rate of 900 fps.

## 6.1 Response to initial conditions

The very first thing I decided to measured was response to initial condition. A smoothed result for a tip displacement movement is in figure 6.4. The initial condition was a deflection from pixel 620 to 1450. By closer inspection of the response I found that the frequency of the tip oscillation is 88 Hz. I also verified the frequency using FFT (*Fast Fourier transform*) in MATLAB.

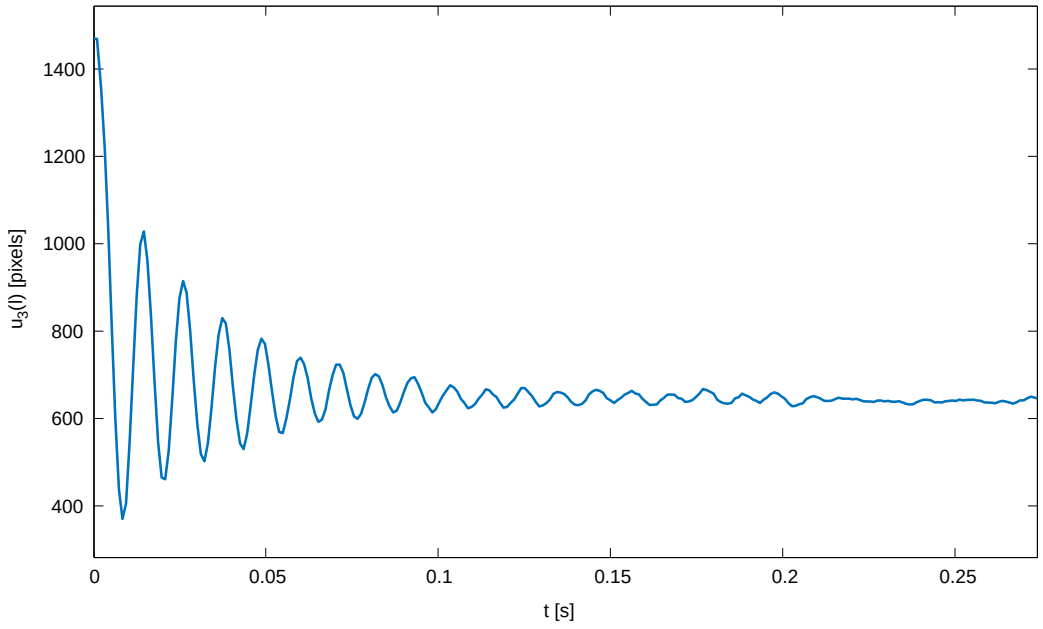


**Figure 6.4.** Tip displacement response to initial conditions (deflection at $t = 0$).

### 6.1.1 Validation of Young's moduli

The oscillatory movement of the tip is certainly the first resonant mode obtained in the dynamic analysis in section 3.3.1.

The weight of the plate which I measured to be

$$m = 21\,\mathrm{g}. \tag{1}$$

and the frequency of 88 Hz can be used to verify the flexural rigidity $EI$ and the Young's moduli respectively. The values were already gotten analytically in section 3.2. For that purpose I need to get the plate's weight per unit length $\rho_l$. From (1) it is

$$\rho_l = \frac{m}{L} = 0.21\,\mathrm{kg{\cdot}m^{-1}}. \tag{2}$$

Following (51) in section 3.3 I indirectly measured $EI$ to be

$$EI = \frac{\rho_l \omega_1^2}{k_1^4} = 0.4118\,\mathrm{N{\cdot}m^2}. \tag{3}$$

| Parameter [units] | Measured value | Analytic value |
|---|---|---|
| $EI$ [N·m$^2$] | 0.4118 | 0.3982 |
| $C$ [N·m] | 6.5363 | 6.3208 |

**Table 6.1.** Comparison of the measured $EI$ and $C$ with values from table 6.1.

### 6.1.2 Damping identification

The same plot (figure 6.4) can be used for the purpose of a damping identification. The speed with which the sinusoid decays is closely related to the damping. I identified the damping ratio $\zeta$ from two local maxima ($y_a = u_3(t_a) - u_3(0)$ and $y_b = u_3(t_b) - u_3(0)$) of the decaying sinusoid, where $t_a < t_b$. The resulting damping is then

$$\zeta = \frac{1}{2\pi n} \ln\left(\frac{y_b}{y_a}\right). \tag{4}$$

The parameter $h$ is the number of periods between the two extrema. The damping ratio is very low for flexible structures, in my case it is

$$\zeta = 0.047. \tag{5}$$

## 6.2 Static deflection

The values from the LC100 were recalculated to convert it from pixels to the tip displacement $u_3(l)$. A small error might have been caused by the camera's noise. The actual point at which the beam reflected was at a distance of 9 cm from the clamped end. The values measured are compared to the values from tables 3.3 and 4.1.

| Voltage $V$ [V] | 10 | 50 | 100 | 200 | 300 |
|---|---|---|---|---|---|
| Measured $u_3$ [$\mu$m] | -45 | -206 | -388 | -825 | — |
| Analytic $u_3$ [$\mu$m] | -41 | -205 | -409 | -818 | -1227 |
| $u_3$ [$\mu$m] (FEM) | -41 | -203 | -406 | -813 | -1220 |

**Table 6.2.** Tip displacement of the cantilever comparison.

## 6.3 Modal response

The dynamic response of the cantilever plate was already simulated using FEM. I could only measure few modes using the line camera as it is able to reconstruct signals only below half of its sampling frequency. I measured the rest by projecting the laser beam onto a paper and watching it wobble. The projected shape of the laser beam was either horizontal or vertical depending on the mode shape. Combined shapes can even make the laser beam running in circles. Different points of the cantilever plate yield different results. There were two points I selected for the measurement, the tip midpoint and the upper tip corner.

Most of the measured modes were identified and they are listed in table 6.3. The modes are listed in the same $(m, n)$ manner as in section 4.3.2. The measured modes are close to those simulated with FEM (figure 4.3) and those gotten from the analytical study (tables 3.6 and 3.5).

| Mode | (1, 1) | (1, 2) | (2, 1) | (3, 1) | (2, 3)[1]) | (4, 1) | (5, 1) |
|---|---|---|---|---|---|---|---|
| $f_n$ [Hz] | 88 | 276 | 550 | 1490 | 2155 | 3100 | 4800 |

**Table 6.3.** Measured modes including their natural frequencies.

## 6.4 Hysteresis

The hysteresis already described in section 5.3 was very hard to measure with my setup due to synchronization problems. The LC100 was badly triggered from Simulink and its response time was shifted against the reference voltage. The synchronization problems resulted in an erroneous behavior — the hysteresis loops measured were thicker for higher frequencies (see figure 6.5). This was not due to the rate-dependence which occurs on much higher frequencies, but due to the phase shift caused by bad synchronization. The hysteresis loops were smoothed to remove noise.

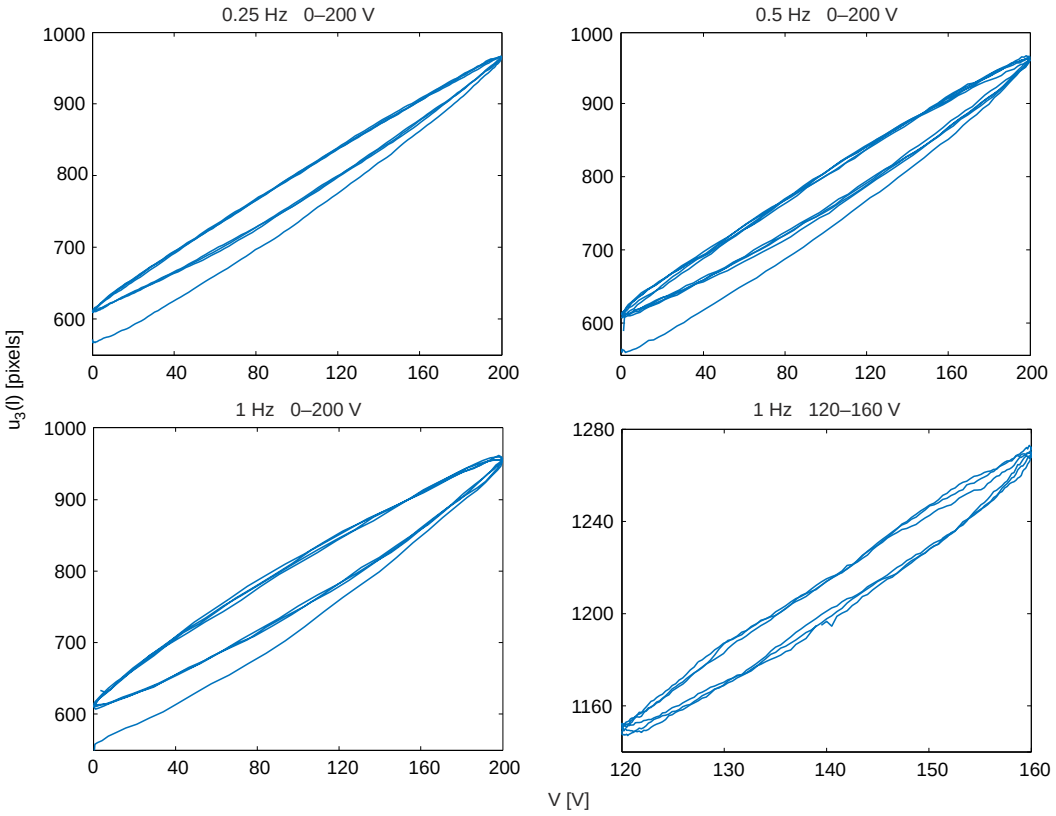


**Figure 6.5.** Hysteresis measured at the tip of the cantilever (unipolar input voltage).

The hysteresis is history-dependent, so it matters what the last state of the material was. The history can be *cleared* by a bipolar decaying sinusoid. I used the one plotted in figure 6.6. The clearing results in the removal of remanent polarization. Three of the graphs in figure 6.5 were obtained measuring the cleared cantilever, these have a loading curve starting at around 550th pixel. The last graph (lower right) does not posses a loading curve, it is a local hysteresis loop for the electrodes voltage of 120–160 V.

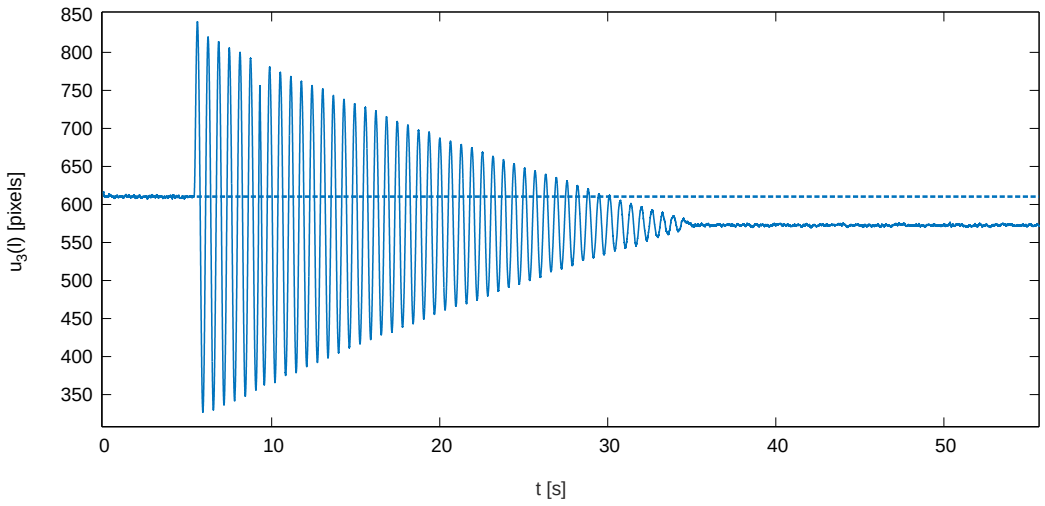


**Figure 6.6.** Clearing the remanent polarization by a linearly decaying sinusoid. The solid line represents the displacement of the tip. The dashed line is the remanent polarization.

I had to use the EPA 104 amplifier for measuring the bipolar hysteresis. The amplifier is not able to deliver more than ±200 V, but I would not even use more in this case because of the depolarization effect (section 5.1). The resulting hysteretic responses for -180–180 V and -100–100 V are shown in figure 6.7.

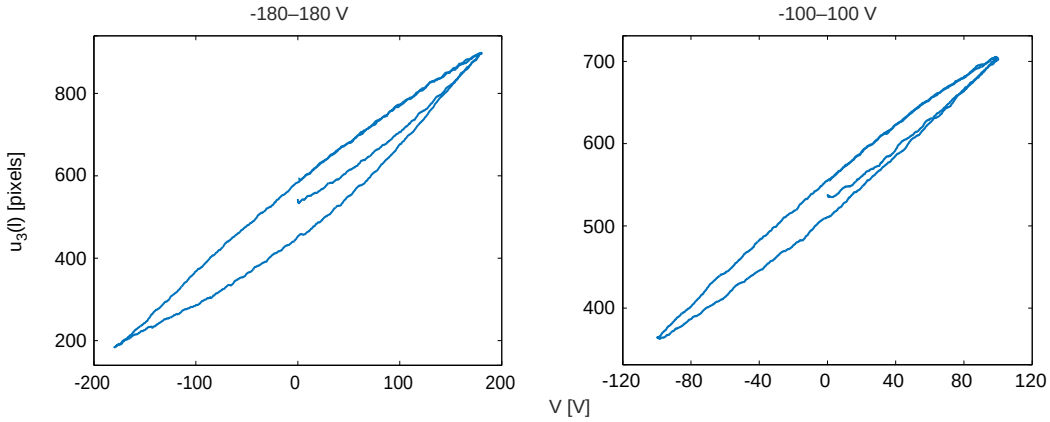


**Figure 6.7.** Hysteresis measured at the tip of the cantilever (bipolar input voltage).

The EPA 104 was not able to supply voltage for the butterfly loop measurement, because of its peak voltage of ±200 V. I had to use the EMCO G05 amplifier in this case. The measurement (figure 6.8) was done almost statically, the voltage change from $-V$ to $+V$ took 1 minute.

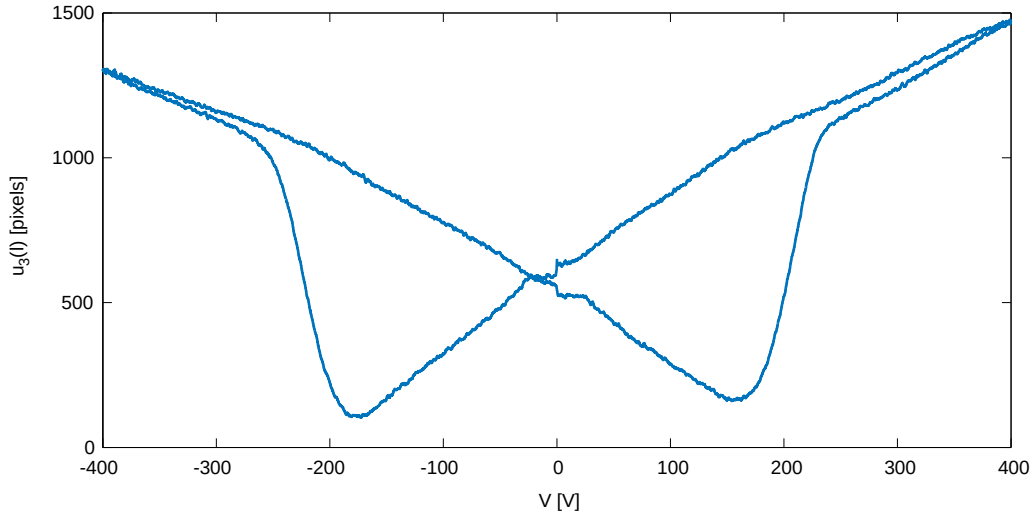


**Figure 6.8.** The measured butterfly loop (voltage on electrodes vs. tip displacement).

## 6.5 Comparison of the amplifiers

The nonlinearity of amplifiers, especially the G05, already mentioned in section 5.4, changes the system's behavior. There are 4 graphs in figure 6.9 demonstrating it. The discharge time takes more than 2 s in the lower left graph, whereas the rise time is only 60 ms. The asymmetry is due to G05 proportionally amplifying both current and voltage. This results in a very large output resistance for very low input voltages. The piezoactuator therefore cannot operate on higher frequencies. It cannot discharge, oscillating around the peak voltage (upper left and lower right plot in figure 6.9).

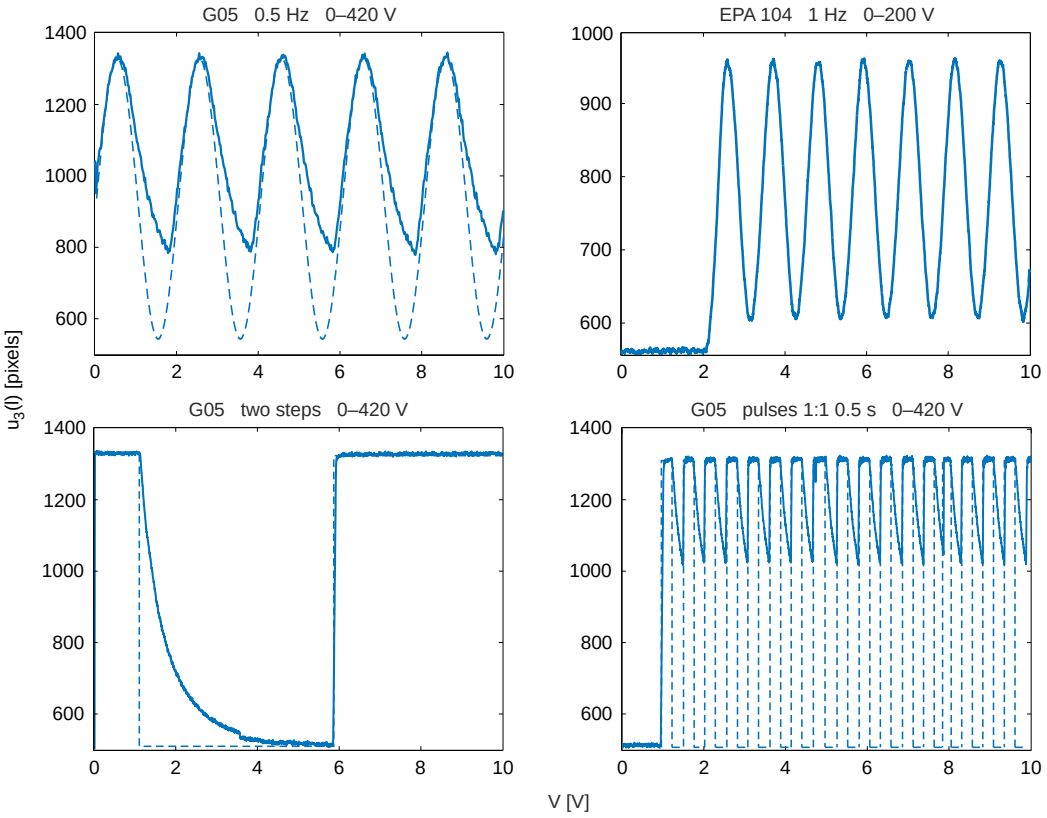


**Figure 6.9.** Four measurements of the voltage amplifier nonlinearity (G05 and EPA 104). Reference signal is the dashed line, output the solid line.

The strong nonlinearity of G05 even results in a very interesting phenomenon. The resonant frequency of 88 Hz as measured and calculated before can be excited by a lower frequency. The reason is the nonlinearity, the way it "kicks" the system when charging the amplifier and the inability to discharge it. I measured such behavior at 44 Hz (half of the resonant frequency), 29 Hz (third) and 22 Hz (quarter). The phenomenon is demonstrated by a chirp signal and a detailed view of the output at the resonance-exciting frequencies (figure 6.10). Another interesting thing is that the curious excitation takes part even with the EPA 104. It is not that apparent as with G05, but still visible even by eye. A linear system would not exhibit such a behavior.

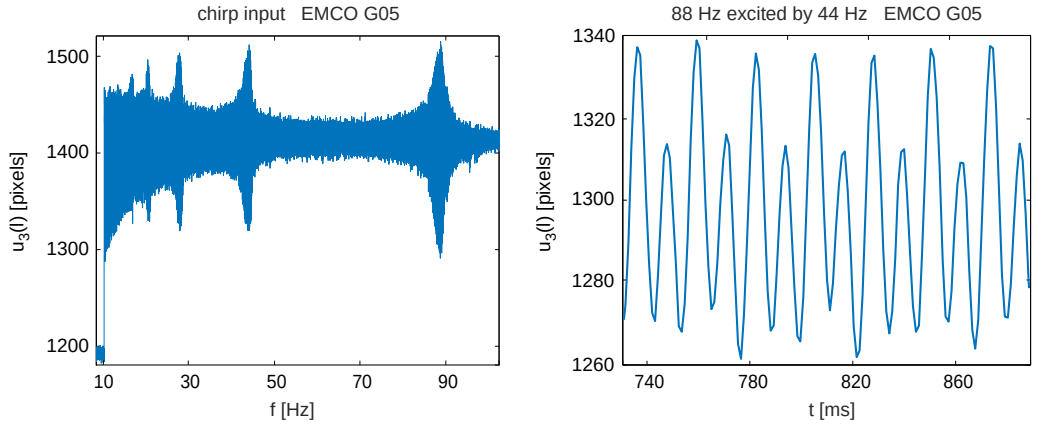


**Figure 6.10.** Resonance excited by lower frequencies as a consequence of the nonlinearities.

# Chapter 7
# Control

The control of active and adaptive optics is among the most discussed long-term goals in optics. A feedforward compensation of nonlinearities like hysteresis and depolarization, which I will briefly mention in section 7.1, is useful to get rid of the actuator's unwanted properties. It is a well maintained topic already and it is among the goals of adaptive and active optics. Adding an nonlinear actuator is actually the controller's problem, but as outlined in the thesis introduction it is the optics that needs to be controlled, not the actuator.

Controlling the optics shape is a challenge. A feedforward controller is not always helpful as it cannot cope with disturbances active and adaptive optics was designed for. The feedforward design might remove the unwanted predictable disturbances, leaving those that are unknown to the controller. To know them a sensor must be included. But how to measure an atmospheric disturbance or flatness of a surface?

There are many solutions for adaptive optics. For example the Shack-Hartman camera or a guided star method for wavefront distortion measurements [28]. But when it comes to topics closer to active optics, feedback is hard to implement. In my case it is the camera, with which I measure one point of the plate. Well enough for measuring the static and dynamic deflection, but not for measuring flatness of the plate. A good idea would be to use the piezoelectric layer (or add another one) as a sensor. It might be suitable for dynamic control, but not suitable for static control due to charge leakage.

I will focus on feedworward control only. I will briefly mention problems that come up with the piezoactuator in section 7.1 and use results from section 3.2 to control shape of the cantilever in section 7.2.

## 7.1 Control of the piezoactuator

As already mentioned the actuator brings nonlinearity to the system. Other than that it is very stable and fast. Its speed depends mostly on the internal resistance of the voltage source. The G05 amplifier is very limiting (section 6.5) and I would not recommend it for control. But the tip deflection can be very fast too, its rise time is in the order of milliseconds. The EPA 104 would do that even faster, but I did not include it into tests in order to avoid destruction of the cantilever.

The problem of the Silicon wafer attached to the actuator is its fragility. An accidental short-circuiting the piezoactuator means actually short-cuircuiting a capacitor, which ideally results in an infinitely large current. That means an infinitely fast change in the strain, so the Si wafer breaks apart.

### 7.1.1 Polarity

The measured data plotted in figure 6.8 confirm the depolarization issue. The piezoelectric actuator should therefore be used in a limited range of input voltages. Only one polarity should be used ideally to avoid problems with depolarization. Accidentally depoling the ceramics results in loosing its original properties (mainly the $d$ constants). To restore it back to its original (catalog) values, the ceramic has to be repoled by applying strong electric field.

### 7.1.2 Compensation of the hysteresis

The measured hysteresis loop from section 6.4 can be compensated with an inverse of the Prandtl-Ishlinskii model [25], [29]. The inverse operator is connected with the plant in series as shown in figure 7.1. It is a feedforward solution, sometimes called the open-loop hysteresis compensation.

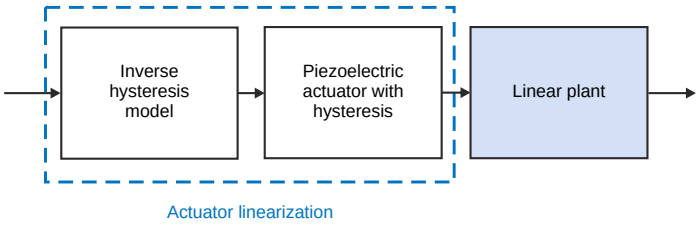


**Figure 7.1.** The feedforward compensation of hysteresis (taken from [25]).

The inverse PI calculated from the PI model from section 5.3.2 and a simulated compensation according to figure 7.1 are shown below in figure 7.2. Note that the inverse operator is almost perfectly compensating the hysteresis, the simulation on the right shows the linear reference-output relation.

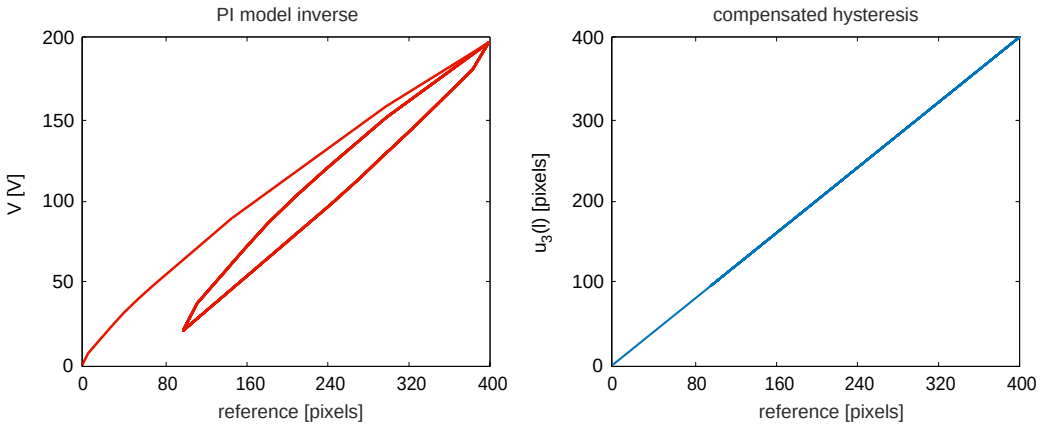


**Figure 7.2.** The inverse PI model on the right, reference-output relation on the left.

## 7.2 Shape control

A reverse analysis of the same problem as in sections 3.2.1 and 3.2.2 can be used to find electric field that would form a desired shape. The shape must be within the range of the actuator and the cantilever itself (i. e. its boundary conditions).

The reverse analysis includes double differentiating with respect to $x$ according to equation (36) in section 3.2. The resulting function of voltage is a second derivative of a desired shape. The lowest possible degree of a polynomial of the desired shape, a second-order polynomial, corresponds to a constant voltage. A cosine shape function results in a cosine function of voltage and so on. A care must be taken though and the boundary conditions have to be considered. The sine function, for example, does not fulfill the boundary conditions in my case. Below is a cosine function I chose for the plate to adapt to:

$$u_3(x) = a\cos\left(\frac{4\pi}{l}x\right) - a, \tag{1}$$

which is also plotted in figure 7.3.

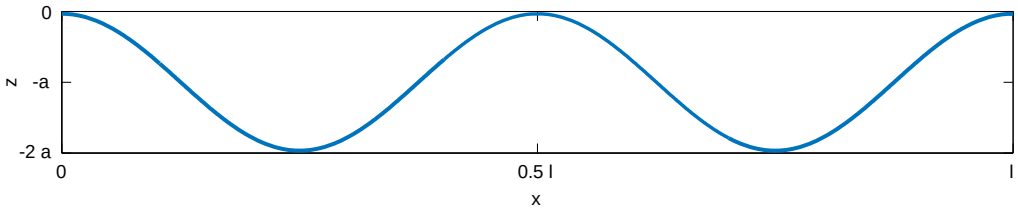


**Figure 7.3.** Desired shape of a simplified cantilever plate fixed at $(x, z) = (0, 0)$.

The equation that needs to be solved is

$$\int_0^l \int_0^l \eta v(x)\, dx\, dx = a\cos\left(\frac{4\pi}{l}x\right) - a. \tag{2}$$

The general solution to (2) is a function of voltage

$$v(x) = -\frac{16\pi^2 a}{\eta l^2}\cos\left(\frac{4\pi}{l}x\right). \tag{3}$$

Such a function can be approximated by a finite number of electrodes. I modified the FEM model used in section 4.3 so that it had 10 electrodes and applied voltage to them according to (3). The voltage was discretized using each electrode's middle point as a reference. The calculated voltage for a chosen $a$ is in table 7.1.

| Electrode | 1 | 2 | 3 | 4 | 5 | 6 | 7 | 8 | 9 | 10 |
|---|---|---|---|---|---|---|---|---|---|---|
| $x$ [mm] | 5 | 15 | 25 | 35 | 45 | 55 | 65 | 75 | 85 | 95 |
| $V$ [V] | -243 | 93 | 300 | 93 | -243 | -243 | 93 | 300 | 93 | -243 |

**Table 7.1.** Calculated voltages $V$ for the 10 electrodes.

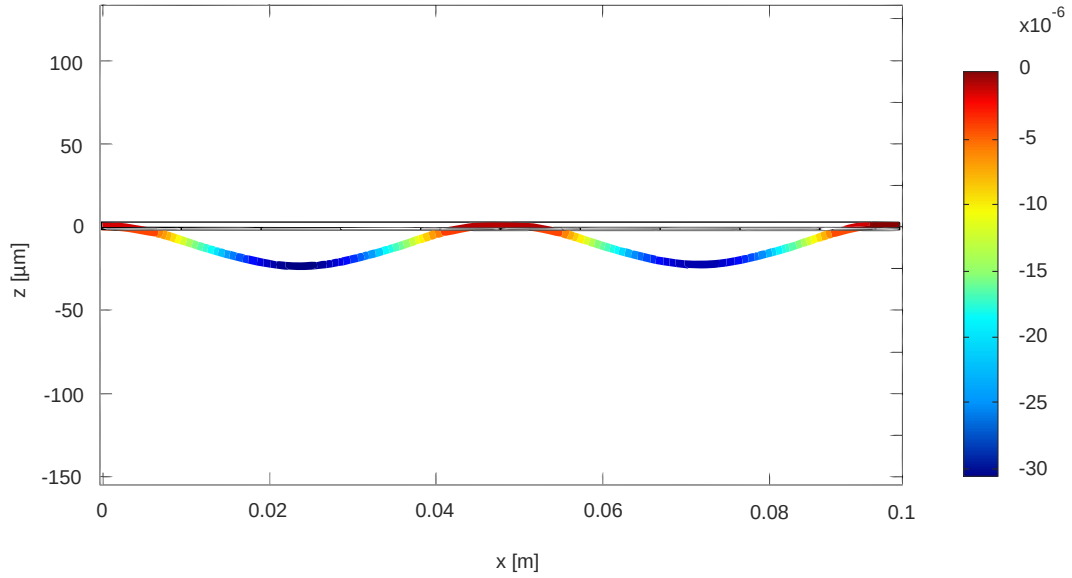


**Figure 7.4.** Deflection of the monomorph cantilever with 10 electrodes (the voltage is applied according to table 7.1).

The case with a fixed end is too constrained, it does only allow few functions that fulfill the boundary conditions. In case of a simply supported structure one could obtain a model for both the cosine and sine functions which can theoretically be combined to obtain any periodic function (spatial Fourier series). Such a result can be used for shaping the mirrors of a KB module (figures 1.1 and 1.2).

# Chapter 8
# Conclusions and future work

Models presented in this thesis offer insight into behavior of the cantilever plate with piezoelectric patches bonded to it. The static analytic model (section 3.2) introduces analysis of bending moments useful for control design purposes. The dynamic model is a result of solving partial differential equations with given boundary conditions. The static model's contribution is the possibility to control shape of the plate by controling the piezo-induced bending moment (I demonstrated it in section 7.2 by presenting a monomorph cantilever with 10 electrodes). The dynamic model completes the understanding by doing the modal decomposition of the plate's motion. I confirmed the static and modal approach by simulating the monomorph plate in Comsol both statically and dynamically. The electrodynamics of the actuator can be neglected to reduce the number of freedoms. Although I managed to find and specify all material parameters (in the form of matrices) needed for FEM and simulate responses correctly, Comsol was unable to export state-space matrices for further use of the models.

Another part of the analysis were the nonlinearities. As mentioned in chapter 5 most of them come from what make the optics adaptive or active. The piezoactuator brings in many nonlinearities, such as creep, hysteresis and depolarization. I therefore made considerations regarding compensation of the unwanted effects in section 7. These include polarity limitations 7.1.1, feedforward hysteresis compensation 7.1.2 and amplifier selection 6.5. Based on it I found the EMCO High Voltage amplifier not suitable for dynamic control.

Measurements presented in chapter 6 matched the simulations, a comparison of the static tip displacements is listed in table 6.2. The measured response of the piezoelectric actuator was very fast. Sudden changes in the reference voltage should be avoided not to destroy the fragile Silicon wafer.

Future work might include a laboratory experiment with the same silicon wafer covered by more electrodes. In case of more than 10 electrodes, the problem of wiring comes up. It could be eliminated by a distributed control. The distributed control might also be used and implemented in the X-ray KB layout (figure 1.1). The feedback control resulting in focused images with minimum distortions is a long-term goal for the team I was lucky to become part of.

# References


[1] V. Maršíková. X-ray optics: Wolter. In *Proceedings of the International Workshop on Astronomical X-Ray Optics, Prague, Czech Republic*, 2009.

[2] A. Safari and E. K. Akdoğan. *Piezoelectric and Acoustic Materials for Transducer Applications*. Springer London, Limited, 2008.

[3] W. Heywang, K. Lubitz, and W. Wersing. *Piezoelectricity: Evolution and Future of a Technology*. Springer series in materials science. Springer Berlin Heidelberg, 2008.

[4] Y. Saito, H. Takao, T. Tani, T. Nonoyama, K. Takatori, T. Homma, T. Nagaya, and M. Nakamura. Lead-free piezoceramics. *Nature*, 432(7013):84–87, 2004.

[5] A. Ballato. Piezoelectricity: Venerable effect, modern thrusts. Technical report, DTIC Document, 1994.

[6] R. B. Williams, Park G., Inman D. J., and Wilkie W. K. An overview of composite actuators with piezoceramic fibers. *Proceeding of IMAC XX*, pages 4–7, 2002.

[7] Smart Material Corp. Piezo fibers and tubes, 2011. Online at: `www.smart-material.com/media/Datasheet/fibers-Version-2011.pdf` [May 2013].

[8] Multifunctional Ceramics Division. Materials for actuators, 2011. Online at: `http://www.ceramtec.com/files/mf_materials-actuators_en_de.pdf` [May 2013].

[9] Inc. Virginia Semiconductor. Basic mechanical and thermal properties of silicon, 2004. Online at `www.virginiasemi.com` [May 2013].

[10] Smart Material Corp. Macro fiber composite, 2011. Online at: `http://www.smart-material.com/media/Datasheet/MFC-V2.0-2011-web.pdf` [May 2013].

[11] IEEE standard on piezoelectricity. *ANSI/IEEE Std 176-1987*, 1988.

[12] D. J. Leo. *Engineering Analysis of Smart Material Systems*. Wiley InterScience. Wiley, 2007.

[13] R. G. Ballas. *Piezoelectric Multilayer Beam Bending Actuators: Static and Dynamic Behavior and Aspects of Sensor Integration*. Microtechnology and MEMS. Springer-Verlag Berlin Heidelberg, 2007.

[14] S. O. R. Moheimani, D. Halim, and A. J. Fleming. *Spatial Control of Vibrations: Theory and Experiments*. A. World Scientific Publishing Company, Incorporated, 2003.

[15] D. J. Gorman. *Free vibration analysis of rectangular plates*. Elsevier, 1982.

[16] R. D. Blevins. *Formulas for Natural Frequency and Mode Shape*. Krieger Publishing Company, 1979.

[17] W. Gawronski. *Advanced Structural Dynamics and Active Control of Structures*. Mechanical Engineering Series. Springer, 2004.

[18] A. Preumont. *Vibration Control of Active Structures: An Introduction*. Solid mechanics and its applications. Springer London, Limited, 2011.

[19] O. M. El-Rifai and K. Youcef-Toumi. Creep in piezoelectric scanners of atomic force microscopes. In *American Control Conference, 2002. Proceedings of the 2002*, volume 5, pages 3777–3782 vol.5, 2002.

[20] C. Zhang, J. Qiu, Y. Chen, and H. Ji. Modeling hysteresis and creep behavior of macrofiber composite–based piezoelectric bimorph actuator. *Journal of Intelligent Material Systems and Structures*, 24(3):369–377, 2013.

[21] R. C. Smith and Z. Ounaies. A domain wall model for hysteresis in piezoelectric materials. *Journal of Intelligent Material Systems and Structures*, 11(1):62–79, 2000.

[22] R. H. Comstock. Charge control of piezoelectric actuators to reduce hysteresis effects, 1981. US Patent 4263527.

[23] M. Špiller and Z. Hurák. Hybrid charge control for stick-slip piezoelectric actuators. *Mechatronics*, 21:100 – 108, 2011.

[24] M. Rakotondrabe. Classical prandtl-ishlinskii modeling and inverse multiplicative structure to compensate hysteresis in piezoactuators. In *American Control Conference (ACC), 2012*, pages 1646–1651, 2012.

[25] Wei-Tech Ang, F. A. Garmon, P. K. Khosla, and C. N. Riviere. Modeling rate-dependent hysteresis in piezoelectric actuators. In *Intelligent Robots and Systems, 2003. (IROS 2003). Proceedings. 2003 IEEE/RSJ International Conference on*, volume 2, pages 1975–1980 vol.2, 2003.

[26] J. Figura. Modeling and control of piezoelectric microactuators. A concurrent bachelor's thesis, 2013.

[27] PI Ceramic. Piezo actuator dynamic operation: Properties, electronics, piezo drivers, 2012. Online at: `www.piceramic.com/pdf/Piezo_Actuator_Dynamic_Operation_Properties_Piezo_Drivers.pdf` [May 2013].

[28] P. Bely. *The Design and Construction of Large Optical Telescopes*. Astronomy and Astrophysics Library. Springer, 2010.

[29] Wei-Tech Ang, P. K. Khosla, and C. N. Riviere. Feedforward controller with inverse rate-dependent model for piezoelectric actuators in trajectory-tracking applications. *Mechatronics, IEEE/ASME Transactions on*, 12(2):134–142, 2007.